ISAS RESEARCH NOTE

ISAS RN 662

Iron Line Diagnostics of the Post-Shock Hot Plasma in Magnetic Cataclysmic Variables Observed with ASCA

Hiroyuki EZUKA and Manabu ISHIDA

THE INSTITUTE OF SPACE AND ASTRONAUTICAL SCIENCE

THE INSTITUTE OF SPACE AND ASTRONAUTICAL SCIENCE
YOSHINODAI, SAGAMIHARA, KANAGAWA 229-8510

ISAS RESEARCH NOTE

ISAS RN 662

Iron Line Diagnostics of the Post-Shock Hot Plasma in Magnetic Cataclysmic Variables Observed with ASCA

Hiroyuki EZUKA and Manabu ISHIDA

August 1998

Institute of Space and Astronautical Science
3-1-1 Yoshinodai, Sagamihara, Kanagawa 229-8510

To appear in the Astrophysical Journal Supplement Series

Iron Line Diagnostics of the Post-Shock Hot Plasma in Magnetic Cataclysmic Variables Observed with ASCA

Hiroyuki Ezuka and Manabu Ishida

Institute of Space and Astronautical Science

3-1-1 Yoshinodai, Sagamihara, Kanagawa 229-8510, Japan

Received _____; accepted _____

ABSTRACT

The *ASCA* spectra of $\sim$ 20 Magnetic Cataclysmic Variables are presented. Owing to the high spectral resolution of the SIS, we successfully resolved the iron $K\alpha$ emission line into the fluorescent (6.4 keV) and the plasma (6.7 and 7.0 keV) components. By comparing the ionization temperature, which is obtained from the intensity ratio of the plasma line components of iron, with the continuum temperature, we have obtained the evidence that the post-shock plasma has a temperature distribution. Detailed analysis indicates that the observed temperature distribution is consistent with that expected from the post-shock plasma model in the bremsstrahlung-cooling domain. In the framework of this post-shock plasma model, we have constrained the mass of the white dwarf in totally nine intermediate polars, and obtained the iron abundances. The obtained masses are generally consistent with the previous X-ray work. We have found that the iron abundance is generally sub-Solar, and its distribution probably peaks at 0.2–0.6$\odot$. We have also shown that the reflection from the white dwarf surface makes significant contribution to the observed the fluorescent iron $K\alpha$ emission line.

Subject headings: accretion, accretion disks — novae, cataclysmic variables — stars: abundances — stars: masses — white dwarfs — X-rays: stars

1. Introduction

Magnetic Cataclysmic Variables (mCVs) are binaries composed of a Roche Lobe filling low mass main sequence star and a magnetized white dwarf. Matter spilt over the Roche Lobe of the main sequence star is funneled by the magnetic field of the white dwarf, and accretes preferentially onto the magnetic pole(s). Since the accretion flow becomes highly supersonic as it approaches the white dwarf, a strong steady shock occurs close to the white dwarf surface, and the accreting matter turns into hot plasma with $T \sim 10^8$ K at the shock front, which radiates hard X-rays.

mCVs have been classified into two categories. One is an intermediate polar (Patterson 1994 and references therein, Hellier 1996) whose emission mainly appears in the hard X-ray band. The white dwarf rotation is faster than the orbital revolution typically by an order of magnitude. The other is a polar (Cropper 1990 and references therein) which mainly emits soft X-ray rather than the hard X-ray. The soft X-ray emission originates from the white dwarf surface, and has the blackbody spectrum with the temperature of 10–60 eV. Another characteristics of the polar is the highly polarized infrared to optical emission. This emission component is considered to be the cyclotron emission in the post-shock hot plasma. Magnetic field of the white dwarf in the polar is so strong (10–60 MG) that the white dwarf rotation and the orbital revolution are synchronized. It has been a matter of debate why the emission spectra of the polar and the intermediate polar are so different. Based on the *ROSAT* observations, Beuermann and Burwitz (1995) indicate that the magnetic field strength plays a crucial role for differentiating the EUV to X-ray emission distribution.

The distinction between the polar and the intermediate polar has been, however, gradually unclear these days in that some polars show a slight asynchronism (V1500 Cyg: Stockman et al.1988, BY Cam: Silber et al.1992, RX J1940.2-1025: Watson et al.1995),

some intermediate polars show polarization in optical (BG CMi: Penning et al.1986, RX J1712–24: Buckley et al.1995, Buckley et al.1997, PQ Gem: Rosen et al.1993), and have the soft X-ray emission (PQ Gem: Mason et al.1992, Duck et al.1994, RX J0558+535 and RX J1914.4+2456: Haberl & Motch 1995).

Matter in the accretion column is considered to fall onto the white dwarf almost radially at the free fall velocity. The temperature of the plasma hence reflects the depth of gravitational potential of the white dwarf and can be written as

$$kT_{\rm S} = \frac{3}{8}\frac{GM}{R}\mu m_{\rm H} = 16\left(\frac{M}{0.5M_{\odot}}\right)\left(\frac{R}{10^9[\rm cm]}\right)^{-1} \quad [\rm keV] \qquad (1)$$

(Aizu 1973) where M and R are the mass and the radius of the white dwarf, μ is the mean molecular weight whose value is 0.615 for Solar abundance plasma, and $m_{\rm H}$ is the mass of hydrogen atom. Below the shock front, the plasma is cooled by the thermal bremsstrahlung in hard X-ray band and the optical cyclotron emission as it descends the column, and settles eventually onto the white dwarf. A number of theoretical models have been proposed to predict the radial profiles of temperature and the density in the post-shock plasma (Hoshi 1973, Aizu 1973, Inoue 1975, Fabian et al.1976, Lamb & Masters 1979, Frank et al.1983, Imamura et al.1987, Wu et al.1994, Wu et al.1995, Woerk & Beuermann 1996). It is generally accepted that the post-shock plasma is cooled by the thermal bremsstrahlung in the intermediate polar (Fujimoto & Ishida 1997) which is believed to have a weaker magnetic field than the polar in general. In this case, the radial profiles of the accretion column is described by Aizu model (Aizu 1973), in which the density, the temperature, and the velocity profiles are analytically solved by combining conservation laws of mass, momentum, and energy including the thermal bremsstrahlung cooling. In the polar, on the other hand, the cyclotron emission is mainly at work close to the shock front, because of the high magnetic field and a probably lower plasma density (Lamb & Masters 1979). Even in the polar, however, the bremsstrahlung cooling gradually dominates the cyclotron cooling

as the plasma descends the accretion column, for the plasma is compressed by the cooling effects. Wu et al. (1994, 1995) derived analytic formula to describe the radial profiles of the post-shock plasma in the polar with various magnetic field strengths and the plasma densities by taking the cyclotron cooling into account.

By measuring the shock temperature, we can set a constraint between the mass and the radius of the white dwarf, as in eq.(1). On the other hand, the mass-radius relation of the white dwarf was well established (Hamada & Salpeter 1961) and a simple analytic formula is obtained by Nauenberg (1972) as

$$R \;=\; 0.78 \times 10^9 \left[\left(\frac{1.44 M_\odot}{M} \right)^{2/3} - \left(\frac{M}{1.44 M_\odot} \right)^{2/3} \right]^{1/2} \quad [\mathrm{cm}] \qquad (2)$$

Therefore, we can evaluate the mass and the radius of the white dwarf separately from eq.(1) and (2) by measuring the shock temperature.

In obtaining the shock temperature, one has to construct a multi-temperature continuum spectrum model according to the theoretical temperature and density profiles of the accretion column, and compare it to the observed spectrum. There are, however, some practical difficulties for this. The continuum spectrum of mCVs in hard X-ray band undergoes a strong photo-electric absorption (Norton & Watson 1989), and it cannot be characterized by a single hydrogen column density. In addition to this, since the shock occurs close to the white dwarf surface, a reflected X-ray emission from the white dwarf surface further complicates the shape of the continuum spectrum (Beardmore et al.1995, Done et al.1995, Done & Magdziarz 1998). These absorption/reflection effects prevent us from measuring the shape of the X-ray continuum precisely. The X-ray spectra of mCVs obtained by *Ginga* (Ishida & Fujimoto 1995, Ishida 1991) can be successfully fitted by a single temperature thermal bremsstrahlung with the temperature of 10–40 keV undergoing multi-column absorption (so-called "partial-covering absorption" model, hereafter we refer to this as PCA model). This fact suggests that the multi-column absorption effect appears

more significantly in the observed spectra than the multi-temperature effect.

In spite of the difficulties, some certain progresses have been made. Cropper et al. (1998) have constructed a continuum model according to the theoretical prediction by Wu et al. (1994, 1995). Assuming a moderately ionized absorber, they successfully fit this model to the *Ginga* spectra of mCVs, and obtained the shock temperature and hence the mass of the white dwarf. Done & Magdziarz (1998) have taken into account $N_{\rm H}$ distribution of the absorber, the reflection, and the temperature distribution of the plasma, and successfully modelled the X-ray spectra of BY Cam.

The SIS onboard *ASCA* has an energy-resolving power ($E/\Delta E = 50$) roughly ten times as great as any detectors so far in orbit, which enable us to discern the iron $K\alpha$ lines of the thermal plasma origin (6.67 keV and 6.97 keV for He-like and hydrogenic iron, respectively) from the fluorescent iron $K\alpha$ line which generally appears at 6.40 keV. The *ASCA* SIS thus provides us with an absolutely new probe to diagnose the hot plasma — measurement of the emission lines. By making use of this high spectral resolution, Hellier, Mukai, & Osborne (1998) already analyzed the iron line spectra of 15 mCVs, and found a broadening of the lines from the plasma probably as a result of the resonance trapping. The emission lines will be of essential importance in improving our understanding of the state of the post-shock plasma in mCVs.

In this paper, we present results of hard X-ray spectroscopy of some 20 mCVs observed by *ASCA*. Since the temperature dependence of the emissivity of the thermal bremsstrahlung and that of the iron line are different, we can expect to obtain different temperatures from the continuum and the lines, if the post-shock plasma really has a temperature distribution as predicted by a number of theories. This would provide us with a new information for investigating the shock temperature and the temperature distribution in the post-shock plasma. In § 2, we describe how the observations were conducted, and

explain the data analysis method. In § 3, we present our results from the iron line and the continuum analysis. We make discussions based on the results in § 4, and provide summaries in § 5.

2. Observation

The *Advanced Satellite for Cosmology and Astrophysics* (*ASCA*) (Tanaka et al.1994) has observed ~30 mCVs since its launch on 1993 Feb 20. *ASCA* is equipped with four equivalent Wolter I type thin foil-nested X-ray telescope modules (XRT; Serlemitsos et al.1995) whose focal length is 3.5 m. Two kinds of detectors are adopted for *ASCA*. One is the SIS (Solid-state Imaging Spectrometer) which adopts X-ray CCD camera (Burke et al.1991, Burke et al.1994, Yamashita et al.1997). The SIS is characterized by its high spectral resolution ($E/\Delta E = 50$ at 5.9 keV) and high sensitivity in lower X-ray energy down to ~0.4 keV. The field of view of the SIS is a square with $11' \times 11'$ in 1-CCD readout mode. The other is the GIS (Gas Imaging Spectrometer) which is a gas scintillation proportional counter (Ohashi et al.1996, Makishima et al.1996). The GIS has a wide field of view (a circle with $25'$ in radius), a high time resolution and a high sensitivity in high energy band up to 10 keV, although its spectral resolution is worse than the SIS by a factor of four. In the common focal plane of the XRTs, two equivalent modules of the SIS and the GIS for each are mounted, which are referred to as SIS0, SIS1, GIS2, and GIS3, respectively.

In this paper, we compile results from observations of 23 targets (29 pointings) from 1993 May to 1996 Oct. All these data are already in the public archive. We have summarized the observation status of each source in table 1.

EDITOR: PLACE TABLE 1 HERE.

All the GIS observations were performed with the Pulse-Height normal mode (PH normal

mode) in which 0.7–10 keV band is covered with 1024 evenly spaced energy channels. On the other hand, the SIS observations are carried out either with Faint mode or Bright mode. These modes cover 0.4–10 keV band with 4096 and 2048 energy channels, respectively. We have made a reduction of the Faint mode data into the Bright mode format before screening the data, only if these two modes coexist in one observation.

In extracting photons from a target, we have adopted a circular aperture centered on the X-ray image of each target, with radii of 4′ and 6′ for the SIS and the GIS, respectively. For background, we have used the entire chip outside the source integration region for the SIS, while an annulus region whose radius is the same as the distance between the boresight of the XRT and the center of the source integration region is used for the GIS.

To obtain spectra of the SIS and the GIS, we have adopted the following data selection criteria. We have discarded data taken when the field of view is within 5° from the earth rim. For the SIS, we have further excluded the data while the field of view is within 20° from the bright earth rim. The data during the spacecraft passing through the SAA are not used. In table 1, we have summarized the effective exposure time and the counting rate for each source after these selections are made. In addition to these selections, we further set one criterion of only accepting the data taken while all the four detectors were normally observing the target simultaneously, in order to combine the spectra of the SIS and the GIS. We then summed the spectra of SIS0 and SIS1 and made the SIS spectrum, and did the same for the GIS spectrum. In fitting the spectra, we combine the SIS and the GIS spectra thus obtained, and fit them simultaneously using XSPEC (v9.01) in XANADU package, although only the SIS spectra will be shown hereafter. The errors quoted hereafter are always those at the 90% confidence level.

3. Analysis and Results

3.1. Iron Emission Lines and Ionization Temperature

We show the spectra of mCVs observed with *ASCA* in the band 5–10 keV in Fig. 1.

EDITOR: PLACE FIGURE 1 HERE.

Because of statistical limit, detailed structure of the iron emission lines are not very clear for some sources. Nevertheless, the fluorescent $K\alpha$ line ($\sim$ 6.4 keV) and the lines from the hot plasma (He-like iron $K\alpha$ line at 6.68 keV and hydrogenic at 6.97 keV) are evidently resolved for some sources (e.g. (h) and (i) AM Her, (j) BY Cam, (n) V1223 Sgr and so on).

In evaluating the intensity of each line component, we have adopted following method. We have first neglected the energy range between 6.0–7.2 keV, and have fitted the spectrum with the thermal bremsstrahlung with the photoelectric absorption. In this fitting, hydrogen column density of the photoelectric absorption is determined solely by the depth of the iron K-edge at $\sim$ 7.1 keV. Then we have retrieved the data points in the band 6.0–7.2 keV, have inserted three Gaussians which represent the fluorescent and the plasma line components, and have fitted the spectrum again. In this spectral fitting, we have fixed all the continuum parameters at the values determined by the continuum fit excluding 6.0–7.2 keV. For the sources with poor statistics, we have constrained the central energy of the hydrogenic $K\alpha$ line to be 1.04 times of that of the He-like line. For some sources, we have also fixed the central energy of the fluorescent iron $K\alpha$ line at 6.40 keV.

The resulting spectral parameters are summarized in table 2.

EDITOR: PLACE TABLE 2 HERE.

The table contains the central energies, intensities, and equivalent widths of the three iron line components, and the ionization temperature ($kT_{\rm ion}$). If the plasma is isothermal and in ionization equilibrium, the intensity ratio of He-like and hydrogenic $K\alpha$ lines is a unique function of the plasma temperature (Mewe et al.1985). This plasma temperature is defined to be the ionization temperature for the given intensity ratio. In mCVs, the obtained ionization temperature gives an average over the entire post-shock plasma if there is a temperature distribution in the plasma (§§ 4.1).

We have also listed in table 2 the hydrogen column density of the absorber ($N_{\rm H,edge}$), the continuum temperature ($kT_{\rm cont}$), and the continuum temperatures measured by *Ginga* ($kT_{\rm ginga}$) (Ishida 1991). The continuum temperatures ($kT_{\rm cont}$) quoted in this table are derived in the next section.

3.2. Continuum Temperature

As described in § 1, the continuum temperature of mCVs observed by *Ginga* distributes in the range 10–40 keV (Ishida & Fujimoto 1995). Thus it seems difficult to evaluate it from the *ASCA* data, because they cover only up to $\sim$ 10 keV. In addition, the multi-column absorption and the reflection from the white dwarf surface makes the temperature evaluation further difficult. If we neglect the absorption/reflection effects and fit the spectrum by the thermal bremsstrahlung with a photoelectric absorption with a single hydrogen column density, resulting temperature becomes higher than the real temperature (Done et al.1995, Done & Magdziarz 1998).

In spite of these difficulties, it is still possible to estimate the continuum temperature from *ASCA* data. The photoelectric absorption in the spectrum of mCVs can be represented

by PCA model as

$$f_O(E) \;=\; \sum_i C_i \exp(-N_{\mathrm{H},i}\sigma(E))\, f_I(E) \qquad (3)$$

where f_I and f_O are the incident and the observed spectra, $\sigma(E)$ is the cross section of the photoelectric absorption by matter with Solar abundance (Morrison & McCammon 1983), $N_{\mathrm{H},i}$ is the hydrogen column density of the $i-$th column, C_i is the covering fraction of the $i-$th column which satisfies

$$\sum_i C_i \;=\; 1.$$

Note that $\sigma(E)$ in eq. (3) varies $\propto E^{-3}$ (Rybicki & Lightman 1979). Therefore, no matter how large $N_{\mathrm{H},i}$ is, there is a critical energy $E_{C,i}$, above which energy

$$N_{\mathrm{H},i}\sigma(E) \;<\; 1 \quad (E > E_{C,i}).$$

In this regime, the exponential term in eq. (3) can be expanded, and eq. (3) is transformed as

$$f_O(E) \;=\; \exp\left(-\left[\sum_i C_i\, N_{\mathrm{H},i}\right]\, \sigma(E)\right) f_I(E) \quad (E > E_C), \qquad (4)$$

by adopting only the leading term, where $E_C = \max[E_{C,1}, E_{C,2}, \ldots]$. Equation (4) thus implies that we can substitute the photoelectric absorption with a single hydrogen column density $\sum_i C_i\, N_{\mathrm{H},i}$ for the PCA model in the energy band above E_C.

The value of E_C, however, should be different from source to source, and it is not known a priori. Therefore we have repeated the spectral fitting by changing the lower boundary (E_{LB}) of the energy band used in the fitting while the upper boundary energy is fixed at 10 keV. In evaluating the continuum temperature, we neglect the band 6.0–7.2 keV in order to avoid the iron emission lines, as in §§ 3.1. Examples of the result are shown in Fig. 2 for AM Her and TV Col.

EDITOR: PLACE FIGURE 2 HERE.

Here we used a single temperature thermal bremsstrahlung for the intrinsic continuum model. If $E_{\rm LB}$ is low enough, the resulting temperature is unrealistically high. This is a result of the hardening of the spectrum due to the multi-column densities described above. As we shift $E_{\rm LB}$ to a higher energy, the resulting temperature goes down and seems to converge to a constant value. This occurs in $E_{\rm LB} \geq 4$ keV ($= E_C$) for both sources in Fig. 2, which is the regime in which the observed spectrum is described by eq.(4). We have adopted $E_{\rm LB}$ which gives the shortest error bar for the temperature in this regime for each source, and have listed in table 2 as $kT_{\rm cont}$, together with that determined from *Ginga* data (Ishida 1991). *Ginga* and *ASCA* temperatures show a reasonable agreement, although the errors of *ASCA* temperatures are larger in general because of a limited energy band.

Note that it is believed that there is a temperature distribution in the post-shock hot plasma, whereas we have adopted the single temperature thermal bremsstrahlung as the continuum model. Therefore the tabulated temperatures should probably be considered as a kind of averaged ones over the entire post-shock plasma. Note also that, although we have taken into account the effect of absorption on the temperature evaluation carefully, it has been pointed out that the resulting average temperature is even reduced if one models the reflection carefully (Done et al.1995, Done & Magdziarz 1998). This point will be discussed in §§ 4.1.

3.3. Line of Sight Absorption

We have attempted to obtain the amount of the line of sight absorption by the spectral fitting. In doing this, we have adopted the following techniques.

1. We have adopted a single temperature thermal bremsstrahlung as a continuum spectral model. The temperature of the thermal bremsstrahlung is fixed basically at

the value measured by *Ginga*, because of its better statistical quality.

2. For the sources for which *ASCA* and *Ginga* temperatures are inconsistent, or *ASCA* measurement has a better statistical quality, or there is no *Ginga* measurement, we have adopted *ASCA* temperature. We have fixed the temperature either at 5, 10, 15, 20 keV closest to the best-fit value obtained by *ASCA* with the method described in §§ 3.2 (table 2).

3. We have modelled the absorber by PCA model basically with two different hydrogen column densities. We have used PCA model with three different column densities, if the two columns is not acceptable at the 90% confidence level, or the three columns are recommended by the F-test. We have assumed Solar abundance for the composition of the absorber (Morrison & McCammon 1983).

4. In the process of the spectral fitting, we have found several emission lines other than those from iron. We have added Gaussians to represent them based on the F-test recommendation.

The results of the fit are shown in Fig. 3. The best fit parameters are listed in table 3.

EDITOR: PLACE FIGURE 3 HERE.

EDITOR: PLACE TABLE 3 HERE.

The table contains adopted temperatures, hydrogen column densities and their covering fractions ($N_{\mathrm{H},i}$ and C_i in eq.(3) and (4)), observed and absorption-corrected fluxes, bolometric luminosities with the distance assumed to be 100 pc ($= 4\pi D^2 F_X$ where

$D = 100$ pc). In addition, for later discussion, we have also tabulated effective hydrogen column density, $N_{\rm H,eff}$, appeared in the bracket of eq.(4)

$$N_{\rm H,eff} = \sum_i C_i N_{{\rm H},i} \tag{5}$$

and the equivalent widths of the fluorescent iron $K\alpha$ line (the same as those in table 2) for easier reference in §§ 4.3.

We summarize some special treatments applied for each source in course of spectral fitting below.

EF Eri — In addition to iron emission lines, He-like and hydrogenic Oxygen lines (0.568 keV and 0.654 keV, respectively) are required. They are significant at more than 99% confidence level from the F-test.

BL Hyi — The spectrum of BL Hyi can be fitted by the photoelectric absorption with a single hydrogen column density, not by PCA-model.

RX J1802.1+1804 — The spectrum of RX J1802+1804 requires a distribution in the plasma temperature rather than in the absorption column density. The only mCV that has been known to show a multi-temperature plasma emission in the continuum spectrum is EX Hya (see below). As in EX Hya, this feature is probably a direct observational evidence of the cooling of the post-shock hot plasma (Ishida et al.1998).

QS Tel — As in BL Hyi, the spectrum can be fitted by a single temperature thermal bremsstrahlung with a single hydrogen column density, although it is possible this is a result of statistical limitation.

EX Hya — The spectrum of EX Hya requires a distribution in the plasma temperature rather than in the absorption column densities. This point is already discussed by several authors (Singh & Swank 1993, Ishida et al.1994a, Ishida et al.1994b, Fujimoto & Ishida 1997). Here we adopt the two temperature thermal bremsstrahlung with a common simple absorber, although the fit is not acceptable ($\chi^2_\nu = 1.88$). EX Hya requires a series of hydrogenic and He-like emission lines from Ne, Mg, Si, S, Ar and Fe, which are also discussed in detail by Fujimoto and ishida (1997).

V1223 Sgr — He-like and hydrogenic $K\alpha$ emission lines from O, Mg, Si and S are necessary to fit the spectrum. All these lines are proved to be significant at more than 90% confidence level from the F-test.

AO Psc — He-like and hydrogenic $K\alpha$ emission lines from O and Si are inserted. They are significant at more than 95% confidence level.

TV Col — He-like and hydrogenic Ne $K\alpha$ lines are significant at more than 99% confidence level.

AE Aqr — As in EX Hya, the spectrum requires two plasma temperatures. We therefore fit the spectrum with two temperature R&S model with the photoelectric absorption with a single hydrogen column density. Note, however, that the white dwarf in AE Aqr rotates so quickly ($P = 33$ s) that the accreting matter is possibly blown away before settling onto the white dwarf surface due to a propeller effect (Wynn & King 1995). It is thus possible that the X-ray emission observed by *ASCA* originates from somewhere close to Alfvén surface. We have added He-like and hydrogenic $K\alpha$ emission lines from Ne, Mg, Si and S.

GK Per in outburst — This is the only source that requires PCA model with four different hydrogen column densities. In addition to this, there is a sign of the soft X-ray component at the lower energy end. This hump can be fitted by the blackbody spectrum with the temperature of 70 eV. It is necessary to include a Gaussian representing He-like Ne $K\alpha$ emission line.

4. Discussion

4.1. Temperature Distribution in the Post-Shock Hot Plasma

In §§ 3.1 and 3.2, we have derived the plasma temperatures measured from the iron emission lines (ionization temperature) and from the continuum (continuum temperature), both of which are listed in table 2. In Fig. 4(a) we have shown a scattered plot between these two temperatures.

EDITOR: PLACE FIGURE 4 HERE.

The dotted line indicates ionization temperature = continuum temperature. Because of limited statistics, each data point is not constrained very well. Nevertheless, it is clear that the ionization temperatures are systematically lower than the continuum temperatures.

Note, however, that the continuum temperatures shown in Fig. 4(a) are probably higher than the true averaged temperatures, because we do not take into account the hardening of the spectrum caused by the reflection explicitly (§§ 3.2). Beardmore et al.(1995) evaluated the temperature of AM Her by the PCA model and the single temperature thermal bremsstrahlung with and without the reflection. The resulting temperatures are 13.5 keV and $\sim$ 20 keV with and without the reflection, respectively (see their table 3). Done et al.(1995) did the same analysis for *Ginga* spectra of EF Eri, and obtained 11 keV and

14.4 keV, respectively. Note that we have mentioned in §§ 3.2 that the *ASCA* temperatures are consistent with those obtained by *Ginga*, which strongly indicates that our analysis underestimates the average continuum temperature. These results, however, suggest that the difference is at the level of 20–40 %. Therefore, we have made the maximum 40 % correction for the continuum temperature of the dotted line, and have drawn as a dot-dash line in Fig. 4(a). Even with respect to the dot-dash line, some 80 % of all the data points still distribute in the area of the lower ionization temperature. Therefore, we consider that the ionization temperature of iron is lower than the continuum temperature collectively, although it is difficult to claim this for the individual sources because of the statistical limitation.

If the post-shock plasma is isothermal and in ionization equilibrium, the ionization temperature and the continuum temperature should be equal. The lower ionization temperature thus indicates at least either one of these two conditions is broken. A well known example of ionization non-equilibrium is a supernova remnant in which the ionization temperature is lower than the continuum temperature in general (Tsunemi et al.1986). Masai (1984) calculated temporal evolution of the ionization distributions of abundant heavy elements immersed in the ambient thermal plasma, and concluded that the elements become in ionization equilibrium with the plasma if $n_e t > 10^{12}\mathrm{cm}^{-3}\mathrm{s}$, where n_e is the electron density, and t is the elapsed time since the matter is shocked. In the post-shock plasma, however, $n_e t$ is estimated to be as great as $\sim 10^{15}\mathrm{cm}^{-3}\mathrm{s}$ (Fujimoto & Ishida 1997), where we adopt the cooling time of the plasma as t. Therefore it is impossible to attribute the lower ionization temperature to the ionization non-equilibrium.

The remaining possibility is thus a temperature distribution in the post-shock hot plasma. As shown in Fujimoto and Ishida (1997), the emissivities of He-like and hydrogenic iron $K\alpha$ lines peak at $kT \sim 5$ keV and ~ 10 keV, respectively. The continuum emissivity

is, on the other hand, proportional to $T^{1/2}$, namely always weighted to higher temperature regions. Therefore, the ionization temperature is expected to be lower than continuum temperature if there is a temperature distribution in the plasma. The observed lower ionization temperature indicates that the post-shock plasma is not uniform and has a temperature distribution.

As a next step, we have attempted to evaluate the temperature distribution quantitatively. As we commented at the end of §§ 3.2, the continuum temperature shown in the abscissa of Fig. 4(a) is not the shock temperature but a kind of the average temperature. In order to obtain the shock temperature from the observed continuum temperature, Wu et al. (1995) developed so-called the "quick fix" method to convert the continuum temperature to the shock temperature, and applied to the *Ginga* data. As mentioned in §§ 3.2, *Ginga* and *ASCA* continuum temperatures are basically consistent. Therefore, we have applied this method to the *ASCA* data, and have plotted the ionization temperature versus the converted shock temperature in Fig. 4(b). Since the X-ray-emitting plasma is considered to be in the bremsstrahlung-cooling domain (Lamb & Masters 1979), we assume $B = 0$ in the process of conversion with the quick-fix method.

We next consider a theoretical relation between the ionization temperature and the shock temperature. In the bremsstrahlung-cooling domain (Lamb & Masters 1979), the radial profiles of the temperature and the density of the post-shock plasma are subject to Aizu model (Aizu 1973, see § 1 also). Combining this with the atomic data table by Mewe et al. (1985), Fujimoto and Ishida (1997) calculated the intensities of hydrogenic and He-like iron $K\alpha$ emission lines (see their eq.(4)) expected from the entire post-shock plasma, and obtained the average ionization temperature as a function of $kT_{\rm S}$ and $kT_{\rm B}$ (see their eq.(5)). In Fig. 4(b) also shown are the relation between the shock temperature and the average ionization temperature thus calculated with $kT_{\rm B} = 0$, 2, and 4 keV. The relation

between the shock temperature and the ionization temperature is not very much affected by the base temperature as long as it is lower than 2 keV. If it is higher than this, the ionization temperature becomes higher for a given shock temperature. This is because the intensity of the He-like iron $K\alpha$ line is more reduced because of a higher base temperature, below which the plasma is considered to be optically thick for the line emission. Although statistical quality of data is not very good, the temperature distribution observed by *ASCA* is consistent with that expected from Aizu model (Aizu 1973). Therefore, we hereafter assume Aizu model for the density and the temperature profiles of the post-shock plasma.

A few remarks are in order here. First, base temperatures have been measured observationally for several sources. They are 0.8 ± 0.2 keV for EX Hya (Fujimoto & Ishida 1997), < 2 keV for AO Psc (Hellier et al.1996), < 0.5 keV for V1223 Sgr (Fujimoto 1996). Therefore it seems reasonable to assume $kT_{\rm B} < 2$ keV hereafter for the post-shock plasma. Second, we have assumed $B = 0$ in converting the continuum temperature into the shock temperature in Fig. 4(b). This is, however, not a good assumption for polars. In polars, the post-shock plasma is believed to be in the cyclotron-cooling domain near the shock front. Therefore, the values of the shock temperature of polars plotted in Fig. 4(b) are not really the shock temperatures but the temperatures at which the bremsstrahlung cooling starts to dominate the cyclotron cooling (Wu et al.1994, Wu et al.1995).

4.2. Mass of the White Dwarf in Intermediate Polars

As described in § 1, we can derive the mass of the white dwarf if the shock temperature is known, with an aid of the mass-radius relation (Nauenberg 1972). Since we have obtained the relation between the shock temperature and the ionization temperature based on Aizu model (shown in Fig. 4(b)), we can obtain a theoretical relation between the mass of the white dwarf and the ionization temperature which is observable, as shown in Fig. 5.

EDITOR: PLACE FIGURE 5 HERE.

Again we show the cases for $kT_{\rm B}$ = 0, 2, and 4 keV. As the base temperature increases, the ionization temperature also increases for a given mass of the white dwarf, because the intensity of He-like iron $K\alpha$ line is more reduced than that of hydrogenic $K\alpha$ line.

By making use of this figure, we can evaluate the mass of the white dwarf from the observed ionization temperature. In table 4, we list the ionization temperatures, which are the same as those listed in table 2, and masses of the white dwarf thus obtained.

EDITOR: PLACE TABLE 4 HERE.

In addition to AO Psc (Hellier et al.1996), EX Hya (Fujimoto & Ishida 1997), and V1223 Sgr (Fujimoto 1996), we have obtained mass constraints for 6 other intermediate polars — RX J1712–24, RX J0558+535, FO Aqr, TV Col, TX Col, and GK Per. As described at the end of §§ 4.1, we have assumed $kT_{\rm B} < 2$ keV, and have used the curve of $kT_{\rm B} = 0$ keV. The ionization temperature of the polars should be regarded as the average only over the bremsstrahlung-cooling domain. Hence we do not tabulate the masses of the polars.

For comparison, we have also tabulated the results of Cropper et al. (1998) who obtained the masses from analysis of the *Ginga* continuum spectra. There are five intermediate polars for which the mass is determined with both methods. Except for TV Col, the results from the other four intermediate polars show a reasonable agreement between the two methods.

The emission line is a local structure in the spectrum, and hence almost free from the complicated absorption/reflection appearing in the continuum spectrum (see § 1). Our line spectroscopy method still suffers from a statistical limitation, and shows somewhat larger errors than those in Cropper et al. (1998). This problem will, however, be resolved in the

near future with a larger effective area in the iron line energy band of *XMM* and *ASTRO-E*.

4.3. Iron Abundances

In Fig. 6(a), we have plotted the equivalent width of the iron emission lines versus the ionization temperature.

EDITOR: PLACE FIGURE 6 HERE.

From a statistical point of view, we have adopted the sum of the equivalent widths of hydrogenic and He-like $K\alpha$ lines.

The continuum intensity from the multi-temperature plasma at the iron line energy can be calculated with the same process as the line emission, just by replacing the line emissivity with the continuum emissivity. The intensity ratio of the line to the continuum gives the theoretical prediction of the equivalent width from the plasma subject to Aizu model. Comparing the observed equivalent width to the prediction, we can evaluate the abundance of iron. In doing this, we have adopted the continuum emissivity model of the optically thin thermal plasma from Mewe et al.(1986), and folded it with the temperature and the density profiles of Aizu model. We then have calculated the theoretical equivalent width as a function of the ionization temperature for the plasma with Solar composition (Morrison & McCammon 1983). The cases of $kT_{\rm B}$ = 0, 2, and 4 keV are also shown in Fig. 6(a). By comparing the data with the curve of $kT_{\rm B}$ = 0 keV, we have obtained the abundances of each mCV, which are listed in table 4. We have found that the iron abundance of mCVs is sub-Solar in general.

The distribution of the iron abundance is shown in Fig. 6(b). Note that we have not considered the error quoted in table 4 and accumulated the data just by referring to the

central values. We have omitted RX J1802+1804 and AE Aqr because of their huge errors. The distribution probably peaks at 0.2–0.6$\odot$.

Note that the post-shock plasma is optically thick for the resonance trapping of the iron $K\alpha$ emission. Done et al. (1995), for example, estimated its optical depth to be 25. One may thus consider this affects the abundance estimation made here. Nevertheless, we believe our conclusion that the iron abundance is sub-Solar needs not to be changed for the following two reasons. First, the electron excited to $2p$ state by trapping the $K\alpha$ photon from other iron atom can be relaxed only by emitting $K\alpha$ photon for He-like and hydrogenic iron. Therefore, the resonance trapping just works as a scattering, and we observe $K\alpha$ photons from the entire post-shock plasma, although they are retarded from the continuum emission. Second, as a result of the optically thick effect, the emergent iron $K\alpha$ photons are no longer isotropic. If the shape of the post-shock accretion region is a geometrically thin slab, for example, they are preferentially emitted upward and downward. However, this effect is probably washed out because our conclusion is derived from evaluation of the rotational phase-averaged spectra of a number of targets. We can thus expect that we have observed the post-shock plasma uniformly from various directions.

Finally, we have to stress again that the sub-Solar abundance is true only "collectively" for mCVs, and one must be careful in estimating the abundance for individual sources by the $K\alpha$ emission line. Recently, some polars are found that show extraordinarily large equivalent width of iron $K\alpha$ emission line such as AX J2315−592 (Misaki et al.1996) and RX J1802+1804 (Ishida et al.1998). A common feature of these two polars is that the accreting pole is always on a visible hemisphere of the white dwarf, and it is expected that we observe them mainly close to a pole-on geometry. Therefore, although it is possible that they really have a high iron abundance, it is also possible that the iron $K\alpha$ emission is enhanced in this direction as a result of the optically thick effect of the resonance trapping.

The latter is possible to be true if the shape of the emission region is a geometrically thin slab.

4.4. Origin of the Fluorescent Iron $K\alpha$ Line

In §§ 3.1 and 3.3, we have evaluated the equivalent width of the fluorescent iron $K\alpha$ line (at 6.4 keV) and the line of sight absorption, respectively. Since the fluorescent iron $K\alpha$ line is emitted via reprocess from matter surrounding the post-shock hot plasma, one can expect some relation between the equivalent width and the line of sight absorption.

Assuming a point-like X-ray source is surrounded by matter with a column density of $N_{\rm H}$ by 4π solid angle, Inoue (1985) derived a simple relation between the equivalent width and $N_{\rm H}$ as

$$EW = \frac{N_{\rm H}}{10^{21}{\rm cm}^{-2}} \quad [{\rm eV}] \tag{6}$$

for the case that the X-ray spectrum is a power-law with the photon index (Γ) of 1.1. As shown in §§3.3, however, thickness of matter surrounding the post-shock plasma is not uniform, for the absorption is represented by PCA model, and the X-ray spectrum is not the power-law but the thermal bremsstrahlung. In this case, eq.(6) is modified as

$$EW = \alpha \sum_i \frac{\Omega_i}{4\pi} \left(\frac{N_{{\rm H},i}}{10^{21}{\rm cm}^{-2}} \right) \quad [{\rm eV}]$$

where α is a correction factor for the X-ray spectral shape. In the case of PCA model, the equivalent width is the sum of contribution from surrounding matter with different thickness, weighted by the solid angle. Here the solid angle should represent a real spatial distribution of matter, although it is impossible to know that in principle, because the accretion-pole geometry with respect to the observer is fixed. Owing to the rotation of the white dwarf, however, we may well assume that the covering fractions evaluated with the phase-average spectra approximately represent the real spatial distribution of matter

surrounding the post-shock plasma, as far as we treat many sources collectively. Then we can set $\Omega_i/4\pi$ equal to the covering fraction of i-th column ($= C_i$) in eq.(3). Hence, the above equation can be transformed using eq.(5) as

$$EW = \alpha \left(\frac{N_{\rm H,eff}}{10^{21}{\rm cm}^{-2}} \right) \quad [{\rm eV}] \tag{7}$$

where $N_{\rm H,eff}$ is listed in table 3.

The correction factor α is obtained as follows. The equivalent width expected for a given incident spectrum f_I satisfies

$$EW \propto \frac{1}{f_I(E_{K\alpha})} \int_{E_{K{\rm edge}}}^{\infty} f_I(E) \sigma_{\rm Fe}(E_{K{\rm edge}}, E) dE, \tag{8}$$

where $E_{K{\rm edge}}$ and $E_{K\alpha}$ are the energies of the iron K-edge and the $K\alpha$ line which are 7.1 and 6.4 keV, respectively. $\sigma_{\rm Fe}(E_{K{\rm edge}}, E)$ is the cross section of the iron K-edge (Reilman & Manson 1978, Reilman & Manson 1979). Since $\alpha = 1$ for the power-law with $\Gamma = 1.1$, α for the thermal bremsstrahlung is obtained as the ratio of eq.(8) with f_I of the thermal bremsstrahlung to that of the power-law with $\Gamma = 1.1$. For the thermal bremsstrahlung spectrum with the temperatures of 10, 15 and 20 keV, α becomes 0.67, 0.74, and 0.78, respectively.

In Fig. 7(a), we have plotted the observed equivalent width ($EW_{\rm obs}$) of the fluorescent iron $K\alpha$ line versus $N_{\rm H,eff}$, both of which are listed in table 3.

EDITOR: PLACE FIGURE 7 HERE.

We have also drawn the expected relation (eq.(7)) with the incident thermal bremsstrahlung spectrum of $kT = 10$ and 20 keV. Although a statistics is limited, we can at least claim that the data points locate above the expected lines on the whole. Since the measured abundance is generally sub-Solar (table 4), whereas the expected relation is calculated

in the case of Solar abundance, this tendency would be more conspicuous if we make a correction for the abundance.

It has been pointed out that the white dwarf surface is probably a non-negligible source of the fluorescent iron $K\alpha$ emission line (Beardmore et al.1995, Done & Magdziarz 1998). Since the reflectivity of the white dwarf surface is not very high (at most 0.3 at 10 keV), the continuum spectral shape is not affected by the reflected component so much. However, the equivalent width of the fluorescent line with respect to the reflected continuum is as great as a few keV (Inoue 1985). Therefore, the fluorescent iron line can appear on the observed continuum with an equivalent width as much as $\sim$100 eV even if the line of sight absorption is negligibly small.

We have thus attempted to explain the amount of the observed equivalent width by the sum of contributions from the line of sight absorber and that from the white dwarf surface. In doing this, we have to make an abundance correction for the white dwarf component to compare different sources with different abundances. Note that this is not necessary for the absorber component, because both the equivalent width and $N_{\rm H}$ scale in proportion to the abundance, and thus eq.(6) holds irrespectively of the abundance. The corrected equivalent width to Solar abundance $EW_{\rm cor}$ of each source is calculated by

$$EW_{\rm cor} = EW_{\rm obs} - (EW(Z) - EW(Z_\odot)) \quad [\rm eV] \tag{9}$$

where $EW_{\rm obs}$ is the observed equivalent width, $EW(Z)$ is the equivalent width expected from the white dwarf surface with the iron abundance of Z. George and Fabian (1991) calculated equivalent widths of $K\alpha$ emission lines from heavy elements in various configurations and abundances of reflectors. They obtained $EW(Z_\odot) = 100$ eV in the case that the reflector subtends 2π solid angle over the thermal bremsstrahlung X-ray source ($kT = 10 - 20$ keV) and the angle between the observer's line of sight and the normal of the reflecting surface is 60°.

In Fig. 7(b), we have plotted $EW_{\rm cor}$ of mCVs versus $N_{\rm H,eff}$. For abundance correction, we have used the values listed in table 4. Some data points for which we are not able to obtain the abundance value are omitted in converting the data from Fig. 7(a). In Fig. 7(b) also drawn are dashed curves which are

$$EW_{\rm cor} = EW(Z_\odot) + \frac{\alpha}{2}\left(\frac{N_{\rm H,eff}}{10^{21}{\rm cm}^{-2}}\right) \quad [{\rm eV}] \tag{10}$$

in which α =0.67 (kT=10 keV) and 0.78 (kT=20 keV). The factor 1/2 in the second term of the right side is introduced, because now we consider that the white dwarf surface occupies 2π solid angle and hence the absorber should be considered to subtend the rest 2π solid angle, not 4π. The data points scatter around the dashed curves representing eq.(10), and indicates that the amount of the observed fluorescent iron $K\alpha$ emission line can be explained by the sum of contributions from the white dwarf surface and the matter in the line of sight. The latter is probably in the pre-shock accretion column. It is particularly important to note that the equivalent width as great as 100 eV is found even from the targets showing a weak absorption $N_{\rm H,eff} \leq 10^{22}{\rm cm}^{-2}$. This is a clear observational evidence that the reflection from the white dwarf generally makes a significant contribution to the fluorescent iron $K\alpha$ line in mCVs.

We would like to make some remarks here. First, some recent works adopt a continuous distribution for the covering fraction of the absorber rather than several discrete values as in PCA-model (Norton et al.1991, Done & Magdziarz 1998). They generally assume that the covering fraction obeys the power-law of $N_{\rm H}$, namely $\propto N_{\rm H}^{-\beta}$. Although a continuous distribution for the covering fraction is probably more realistic, the absorption structure is really complex and it is difficult to predict the distribution function of the covering fraction. Generally, the maximum column in the continuous distribution model is larger than the greatest column in PCA model. Both models can be, however, consistent because PCA model samples the continuous distribution of the column with a limited number of discrete

columns.

Second, recent works (including this paper) have started to show that there is a temperature distribution in the post-shock plasma (Fujimoto & Ishida 1997, Done & Magdziarz 1998, Ishida et al.1998). One of the differences of the multi-temperature plasma emission from a single temperature one is that the spectrum is softer in a lower energy band. If a single temperature thermal bremsstrahlung model with the absorption is applied to this multi-temperature plasma emission spectrum, one may expect that $N_{\rm H}$ is underestimated. However, Done et al.(1995) show that the continuum shape of the single temperature thermal bremsstrahlung and the multi-temperature one is small in the band below 10 keV, and hence the underestimation of $N_{\rm H}$ is expected to be small. As a matter of fact, although the covering fraction and the hydrogen column density of each PCA component (C_i and $N_{{\rm H},i}$ in eq.(4)) slightly alter if we substitute so-called Boltzmann model spectrum

$$F(E) \;=\; A \cdot E^{-\Gamma} e^{-E/kT},$$

which can mimic the multi-temperature thermal bremsstrahlung, for the thermal bremsstrahlung, resulting effective hydrogen column density ($N_{\rm H,eff}$: eq.(4)), which is the key parameter to predict the equivalent width in eq.(7), does not change more than ~ 10 %. This is because $N_{\rm H,eff}$ is determined in the fitting mainly by the depth of the iron K-edge at 7.1 keV. Since this is a local structure in the continuum spectrum, $N_{\rm H,eff}$ becomes free from overall spectral shape.

Finally, we consider the effect of the reflected continuum on the evaluation of $N_{\rm H,eff}$ which has so far been assumed to originate solely from the matter in the line of sight. Although the intensity of the reflected continuum is at most of order ~ 0.1 of that of the direct component, it shows a strong iron K-edge in its spectrum, which may affect our estimation of the line of sight $N_{\rm H,eff}$. We have thus attempted to perform a spectral simulation with "fakeit" command in the XSPEC package. As an incident spectral model,

we have assumed a power-law with $\Gamma = 1.3$ undergoing the photoelectric absorption with a single hydrogen column density $N_{\rm H,cloud}$. We have added to this a component reflected from the white dwarf surface with Solar abundance ("plrefl" model in XSPEC). Here we have assumed that the white dwarf surface subtends 2π solid angle, and the angle between the line of sight and the normal of the surface is 60°. We then have made simulated spectra for various $N_{\rm H,cloud}$ which includes totally 500,000 photons for each, fitted it by the power-law with PCA model, and obtained resulting $N_{\rm H,eff}$ according to eq.(5). In Fig. 8, we show a relation between $N_{\rm H,cloud}$ and $N_{\rm H,eff}$.

EDITOR: PLACE FIGURE 8 HERE.

It is now revealed that the observed $N_{\rm H,eff}$ probably includes an offset of $10^{22}{\rm cm}^{-2}$ brought about by the continuum reflected from the white dwarf surface. Equation (7) indicates, however, that this offset amounts only to several eV in the equivalent width. Thus we consider it is effectively not necessary to make any correction to the relation between the equivalent width and $N_{\rm H,eff}$ (Fig. 7).

5. Conclusion

We have presented *ASCA* data of $\sim$ 20 mCVs, with a particular stress on the iron emission lines. The high spectral resolution of the *ASCA* SIS enables us to resolve the hydrogenic and He-like iron $K\alpha$ emission lines. The intensity ratio of these two line components provides us with a completely new probe to diagnose the post-shock hot plasma, namely the ionization temperature. Since the temperature dependence of the volume emissivity is different between the continuum and the lines, the continuum temperature and the ionization temperature are different if the plasma has a temperature distribution. The *ASCA* observations really show that the ionization temperatures are lower than the

continuum temperatures in general, which is the first clear observational evidence of the existence of a temperature distribution in the post-shock hot plasma. From a detailed analysis, we have shown that the observed relation between the continuum temperature and the ionization temperature is consistent with that expected from the post-shock plasma being cooled by the optically thin thermal plasma emission (Aizu 1973).

In the framework of Aizu model, we have set constraint on the masses of 9 intermediate polars (see also Hellier et al.1996, Fujimoto & Ishida 1997, Fujimoto 1996) with our line spectroscopy method. We have compared the masses obtained here and those from Cropper et al. (1998) who derived the masses by evaluating the *Ginga* continuum spectra, and found reasonable agreements between them.

Within the framework of Aizu mode, we can obtain the expected equivalent width of the iron $K\alpha$ lines. By comparing this to that observed, we have evaluated the iron abundances of mCVs observed by *ASCA*. We have shown that the iron abundances of mCVs are generally sub-Solar, and the distribution probably peaks at 0.2–0.6$\odot$.

The *ASCA* SIS can also resolve the fluorescent iron $K\alpha$ emission line from the plasma iron line components. We have investigated the equivalent width of the fluorescence component in relation with the line of sight absorption. The equivalent widths as great as $\sim$ 100 eV are found even from sources whose spectra show the absorption with $N_{\rm H}$ smaller than $10^{22}{\rm cm}^{-2}$. Detailed analysis indicates that the reflection from the white dwarf surface makes significant contribution to the observed fluorescent iron $K\alpha$ line.

REFERENCES

Aizu K. 1973, Progr. Theoret. Phys., 49, 1184

Beardmore A. P., Done C., Osborne J. P., & Ishida M. 1995, MNRAS, 272, 749

Beuermann K., & Burwitz V. 1995, in Cape Workshop on Magnetic Cataclysmic Variables, ASP Conference Series, Vol. 85, eds. D. A. H. Buckley & B. Warner, (San Francisco:ASP), 99

Buckley D. A. H. et al. 1995, MNRAS, 275, 1028

Buckley D. A. H., Haberl F., Motch C., Pollard K., Schwarzenberg-Czerny A., & Sekiguchi K. 1997, MNRAS, 287, 117

Burke B. E. et al. 1991, IEEE Trans. Nucl. Sci. 38, 1069

Burke B. E. et al. 1994, IEEE Trans. Nucl. Sci. 41, 375

Cropper M. 1990, Sp. Sci. Rev. 54, 195

Cropper M., Ramsay G., & Wu K. 1998, MNRAS, 293, 222

Done C., Osborne J. P., & Beardmore A. P. 1995, MNRAS, 276, 483

Done C., & Magdziarz P. 1998, MNRAS, *accepted*

Duck S. R., Rosen S. R., Ponman T. J., Norton A. J., Watson M. G., & Mason K. O. 1994, MNRAS, 271, 372

Fabian A. C., Pringle J. E., & Rees M. J. 1976, MNRAS, 175, 43

Frank J., King A. R., & Lasota J. P. 1983, MNRAS, 202, 183

Fujimoto R., & Ishida M. 1997, ApJ, 474, 774

Fujimoto R., 1996, Ph.D. Thesis, University of Tokyo

George I. M., & Fabian A. C. 1991, MNRAS, 249, 352

Haberl F., & Motch C. 1995, A&A, 297, L37

Hamada T., & Salpeter E. E. 1961, ApJ, 134, 683

Hellier C., 1996, in Cataclysmic Variables and Related Objects, eds. A. Evans & J. Wood, (Holland:Kluwer), 143

Hellier C., Mukai K., Ishida M., & Fujimoto R. 1996, MNRAS, 280, 877

Hellier C., Mukai K., & Osborne J. P. 1998, MNRAS, *accepted*

Hoshi R. 1973, Progr. Theoret. Phys. 49, 776

Imamura J. N., Durisen R. H., Lamb D. Q., & Weast G. J. 1987, ApJ, 313, 298

Inoue H. 1975, PASJ, 27, 311

Inoue H. 1985, Sp. Sci. Rev. 40, 317

Ishida M. 1991, Ph.D. Thesis, University of Tokyo

Ishida M., Makishima K., Mukai K., & Masai K. 1994, MNRAS, 266, 367

Ishida M., Mukai K., & Osborne J. P. 1994, PASJ, 46, L81

Ishida M. & Fujimoto R. 1995, in Cataclysmic Variables, eds. A. Bianchini, M. Della Valle and M. Orio, (Holland:Kluwer), 93

Ishida M., Matsuzaki K., Fujimoto R., Mukai K., & Osborne J. P. 1997, MNRAS, 287, 651

Ishida M., Greiner J. C., Remillard R. A., & Motch C. 1998, A&A, 335, 200

Kallman T. R., Mukai K., Schlegel E. M., & Paerels F. B. 1996, ApJ, 466, 973

Lamb D. Q., & Masters A. R. 1979, ApJ, 234, L117

Makishima K. et al. 1996, PASJ, 48, 171

Masai K. 1984, Ap&SS, 98, 367

Mason K. O. et al. 1992, MNRAS, 258, 749

Mason K. O. 1997, MNRAS, 285, 493

Mewe R., Gronenschild E. H. B. M., & van den Oord G. H. J. 1985, A&A Suppl., 62, 197

Mewe R., Lemen J. R., & van den Oord G. H. J. 1986, A&A Suppl., 65, 511

Misaki K., Terashima Y., Kamata Y., Ishida M., Kunieda H., & Tawara Y. 1996, ApJ 470, L53

Morrison R., & McCammon D. 1983, ApJ, 270, 119

Mukai K., Ishida M., & Osborne J. P. 1994, PASJ, 46, L87

Nauenberg M. 1972, ApJ, 175, 417

Norton A. J., & Watson M. G. 1989, MNRAS, 237, 853

Norton A. J., Watson M. G., & King A. R. 1991, in Iron Line Diagnostics in X-ray Sources, Lecture Notes on Physics Vol. 385, eds. A. Treves, G. C. Perola and L. Stella (Berlin:Springer), 155

Norton A. J., Hellier C., Beardmore A. P., Wheatley P., Osborne J. P., & Taylor P. 1997, MNRAS, 289, 362

Ohashi T. et al. 1996, PASJ, 48, 157

Osborne J. P., Ishida M., and Mukai K. 1994, in New Horizon of X-ray Astronomy, eds. F. Makino & T. Ohashi (Tokyo:Universal Academy Press) 401

Osborne J. P., Beardmore A. P., Done C., Ishida M., and Mukai K. 1995, in Cape Workshop on Magnetic Cataclysmic Variables, ASP Conference Series Vol. 85, ed. D. A. H. Buckley and B. Warner (San Francisco:ASP), 128

Patterson J. 1994, PASP, 106, 209

Penning W. R., Schmidt G. D., & Liebert J. 1986, ApJ, 301, 885

Reilman R. F., & Manson S. T. 1978, Phys. Rev. A, 18, 2124

— 1979, ApJS, 40, 815

Rosen S. R., Mittaz J. P. D., & Hakala P. J. 1993, MNRAS, 264, 171

Rybicki G. B., & Lightman A. P., 1979, Radiative Processes in Astrophysics (New York:Wiley), 282

Serlemitsos P. J. et al. 1995, PASJ, 47, 105

Silber A., Bradt H. V., Ishida M., Ohashi T., & Remillard R. A. 1992, ApJ, 389, 704

Singh J., & Swank J. 1993, MNRAS, 262, 1000

Stockman H. S., Schmidt G. D., & Lamb D. Q. 1988, ApJ, 332, 282

Tanaka Y., Inoue H., & Holt S. S. 1994, PASJ, 46, L37

Tsunemi H., Yamashita K., Masai K., Hayakawa S., & Koyama K. 1986, ApJ, 306, 248

Watson M. G., Rosen S. R., O'Donoghue D., Buckley D. A. H., Warner B., Hellier C., Ramseyer T., Done C., & Madejski J. 1995, MNRAS, 273, 681

Woerk U., & Beuermann K. 1996, A&A, 306, 232

Wu K., Chanmugan G., & Shaviv G. 1994, ApJ, 426, 664

Wu K., Chanmugan G., & Shaviv G. 1995, ApJ, 455, 260

Wynn G. A., & King A. R. 1995, MNRAS, 275, 9

Yamashita A. et al. 1997, IEEE Trans. Nucl. Sci. 44, 847

This manuscript was prepared with the AAS LaTeX macros v4.0.

TABLE 1

OBSERVATION LOG OF MCVs

Source		Date (UT)	DP Mode		Exposure (ks)[a]		Count Rate (c/s)[a,b]		PI[c]	Ref
			SIS	GIS	SIS	GIS	SIS	GIS		
Polars										
EF Eri		1993/07/23.90–24.77	Faint	PH Normal	35.9	39.0	0.927	0.613	Ishida	[1, 2]
VV Pup		1993/11/14.92–16.12	Faint	PH Normal	47.5	47.9	0.050	0.039	Ishida	
V834 Cen		1994/03/03.64–04.13	Faint	PH Normal	21.7	23.2	0.258	0.183	Mukai	
RXJ1802+1804		1996/09/30.71–02.97	Faint/Bright	PH Normal	71.3	75.6	0.040	0.032	Ishida	
BL Hyi		1994/10/11.47–12.59	Faint	PH Normal	41.4	43.5	0.212	0.158	Fujimoto	
RX2107–05		1994/11/03.77–04.29	Faint/Bright	PH Normal	21.8	23.3	0.048	0.040	Schlegel	
QS Tel		1996/09/28.91–29.57	Faint	PH Normal	16.8	17.7	0.056	0.046	Rosen	
AM Her	1)	1993/09/27.22–28.27	Faint/Bright	PH Normal	42.0	42.8	0.608	0.427	Gotthelf	[2, 3]
	2)	1995/03/06.84–07.22	Faint	PH Normal	17.7	18.4	0.911	0.658	Ishida	
	3)	1995/03/09.03–10.03	Faint	PH Normal	42.9	45.7	0.889	0.653	Ishida	
BY Cam		1994/03/11.49–12.16	Faint	PH Normal	26.9	29.6	0.960	0.668	Kallman	[4, 5]
QQ Vul		1994/10/23.79–24.46	Faint/Bright	PH Normal	25.9	27.0	0.078	0.065	Mukai	
Intermediate Polars										
EX Hya		1993/07/16.45–17.64	Faint	PH Normal	36.0	38.8	2.79	1.50	Ishida	[6, 7, 8]
BG CMi	1)	1996/04/14.76–15.97	Faint/Bright	PH Normal	42.0	43.4	0.157	0.169	Mukai	
	2)	1996/04/17.44–18.53	Faint/Bright	PH Normal	40.9	41.5	0.145	0.161	Mukai	
V1223 Sgr		1994/04/24.18–25.96	Faint	PH Normal	57.0	59.2	1.23	1.00	Osborne	[6]
RX1712–24		1996/03/18.85–21.24	Faint/Bright	PH Normal	81.4	84.2	0.788	0.654	Hellier	
AO Psc		1994/06/22.29–24.56	Faint/Bright	PH Normal	81.0	84.3	0.537	0.480	Hellier	[6, 9]
RXJ0558+535		1996/10/05.57–07.48	Faint/Bright	PH Normal	76.3	82.0	0.327	0.241	Mukai	
FO Aqr		1993/05/20.93–22.04	Faint/Bright	PH Normal	37.8	38.0	0.266	0.317	Mukai	[10]
RE0751+14		1994/11/04.91–07.10	Faint	PH Normal	76.2	80.2	0.365	0.298	Fujimoto	[11]
TV Col		1995/02/28.25–01.44	Faint/Bright	PH Normal	36.7	39.9	0.648	0.542	Mauche	
TX Col		1994/10/03.29–04.42	Faint	PH Normal	39.9	45.1	0.221	0.161	Wheatley	[12]
XY Ari	1)	1995/08/07.00–07.91	Faint	PH Normal	34.6	34.9	0.143	0.147	Schlegel	
	2)	1996/01/28.21–29.73	Faint	PH Normal	58.5	61.0	0.155	0.161	Ishida	
	3)	1996/02/18.97–19.56	Faint	PH Normal	24.4	25.6	0.130	0.137	Ishida	
AE Aqr		1995/10/14.01–14.96	Faint/Bright	PH Normal	41.6	43.5	0.305	0.150	Bookbinder	
GK Per (Qui.)		1995/02/04.40–05.47	Faint/Bright	PH Normal	41.6	41.6	0.368	0.357	Mauche	
GK Per (Outb.)		1996/03/04.27–04.87	Faint	PH Normal	24.0	23.7	1.21	1.24	Ishida (TOO)	

[a]Average of SIS 0 and SIS 1, and GIS 2 and GIS 3 for the SIS and GIS, respectively.

[b]0.4–10.0 keV for the SIS, and 0.7–10.0 keV for the GIS. The aperture radius is 4 arcmin and 6 arcmin for the SIS and GIS, respectively.

[c]Principal Investigator (TOO = Target Of Opportunity).

REFERENCES.— [1] Osborne *et al.* (1994); [2] Osborne *et al.* (1995); [3] Ishida *et al.* (1997); [4] Done and Magdziarz (1998); [5] Kallman *et al.* (1996); [6] Fujimoto (1996); [7] Fujimoto and Ishida (1997); [8] Ishida *et al.* (1994); [9] Hellier *et al.* (1996); [10] Mukai *et al.* (1994); [11] Mason (1997); [12] Norton *et al.* (1997)

TABLE 2

BEST FIT PARAMETERS IN THE BAND 5–10 KEV BY THE MODEL OF THE THERMAL BREMSSTRAHLUNG WITH THREE GAUSSIANS.

Source	Line Center Energy [keV]			Line Intensity[a]			Equivalent Width [eV]			$kT_{\rm ion}$[d]	$N_{\rm H,edge}$[e]	$kT_{\rm cont}$[f]	$kT_{\rm ginga}$[g]
	Fluo.	He-like	H-like	Fluo.	He-like	H-like	Fluo.	He-like	H-like	[keV]	[10^{22} cm^{-2}]	[keV]	[keV]
Polars													
EF Eri	6.40^{b}	$6.72^{+0.06}_{-0.06}$	$6.96^{+0.12}_{-0.12}$	$1.8^{+1.9}_{-1.8}$	$5.6^{+2.4}_{-2.6}$	$2.9^{+2.4}_{-2.3}$	30^{+32}_{-30}	100^{+43}_{-47}	57^{+47}_{-47}	$8.8^{+3.9}_{-5.5}$	$2.5^{+4.8}_{-2.5}$	19^{+14}_{-6}	16.9 ± 0.6
VV Pup	6.40^{b}	6.69^{b}	6.96^{c}	$0.24^{+0.79}_{-0.24}$	< 0.86	$0.15^{+0.71}_{-0.15}$	150^{+480}_{-150}	< 570	120^{+490}_{-120}	—	11^{+52}_{-11}	17^{+25}_{-8}	—
V834 Cen	6.40^{b}	$6.69^{+0.05}_{-0.32}$	$6.96^{+0.05c}_{-0.33}$	$0.95^{+1.62}_{-0.95}$	$4.3^{+2.0}_{-2.2}$	$0.47^{+2.37}_{-0.47}$	79^{+135}_{-79}	390^{+190}_{-200}	47^{+236}_{-47}	$4.5^{+5.3}_{-4.5}$	$1.9^{+19.5}_{-1.9}$	30^{+34}_{-18}	14.7 ± 1.3
RXJ1802+1804	6.40^{b}	$6.73^{+0.24}_{-0.24}$	$7.00^{+0.25c}_{-0.25}$	$0.49^{+0.31}_{-0.49}$	$1.0^{+0.8}_{-1.0}$	$0.26^{+1.58}_{-0.26}$	1300^{+1300}_{-1300}	3200^{+3600}_{-3200}	1000^{+6000}_{-1000}	$6.4^{+12.5}_{-6.4}$	$20^{+\infty}_{-20}$	$4.4^{+41.8}_{-3.2}$	—
BL Hyi	6.40^{b}	$6.70^{+0.15}_{-0.15}$	$6.97^{+0.15}_{-0.15}$	$0.83^{+0.88}_{-0.83}$	$3.0^{+1.3}_{-2.1}$	$1.8^{+1.9}_{-1.4}$	96^{+103}_{-96}	380^{+170}_{-260}	240^{+240}_{-180}	$9.4^{+5.6}_{-5.4}$	10^{+14}_{-10}	22^{+10}_{-7}	13.2 ± 1.3
RX2107–05	6.40^{b}	6.62^{b}	6.88^{c}	$0.98^{+1.15}_{-0.98}$	< 2.0	$0.30^{+1.27}_{-0.30}$	530^{+650}_{-530}	< 1200	190^{+790}_{-190}	—	$1.6^{+86.9}_{-1.6}$	$11^{+\infty}_{-6}$	—
QS Tel	6.40^{b}	6.69^{b}	6.96^{c}	< 2.4	< 2.7	$0.39^{+3.3}_{-0.39}$	< 3300	< 4100	660^{+5600}_{-660}	—	$7.5^{+\infty}_{-7.5}$	$5.4^{+9.6}_{-3.0}$	—
AM Her (93/09)	$6.41^{+0.03}_{-0.03}$	$6.67^{+0.03}_{-0.03}$	$6.93^{+0.05}_{-0.05}$	13^{+3}_{-3}	12^{+3}_{-3}	$7.8^{+2.9}_{-3.0}$	170^{+40}_{-40}	170^{+40}_{-40}	110^{+40}_{-40}	$9.6^{+2.2}_{-2.5}$	22^{+5}_{-5}	$9.4^{+9.1}_{-3.1}$	18.1 ± 0.4[h]
AM Her (95/03)	$6.42^{+0.02}_{-0.02}$	$6.71^{+0.03}_{-0.03}$	$6.99^{+0.04}_{-0.04}$	18^{+2}_{-2}	17^{+3}_{-3}	9.7^{+2}_{-2}	220^{+30}_{-30}	220^{+30}_{-30}	140^{+40}_{-40}	$9.1^{+1.4}_{-1.5}$	10^{+3}_{-3}	22^{+16}_{-7}	18.1 ± 0.4[h]
BY Cam	$6.38^{+0.07}_{-0.06}$	$6.70^{+0.11}_{-0.11}$	$6.98^{+0.09}_{-0.09}$	$5.0^{+2.0}_{-2.1}$	$3.3^{+2.4}_{-2.6}$	$5.0^{+2.5}_{-4.2}$	81^{+33}_{-34}	58^{+42}_{-45}	93^{+48}_{-79}	16^{+10}_{-11}	$0.69^{+4.70}_{-0.69}$	16^{+18}_{-6}	30.0 ± 4.5
QQ Vul	6.40^{b}	$6.55^{+0.24}_{-0.26}$	$6.81^{+0.25c}_{-0.27}$	$0.19^{+1.78}_{-0.19}$	$2.1^{+1.4}_{-2.0}$	$1.2^{+1.9}_{-1.2}$	54^{+513}_{-54}	630^{+450}_{-630}	410^{+650}_{-410}	$9.3^{+8.2}_{-9.3}$	< 26	$16^{+\infty}_{-13}$	41.9 ± 8.4
Intermediate Polars													
EX Hya	$6.46^{+0.09}_{-0.07}$	$6.67^{+0.02}_{-0.01}$	$6.95^{+0.03}_{-0.03}$	$6.6^{+5.1}_{-2.6}$	28^{+4}_{-5}	10^{+2}_{-2}	91^{+71}_{-36}	350^{+40}_{-60}	140^{+30}_{-30}	$7.4^{+0.9}_{-0.9}$	< 2.9	13^{+5}_{-3}	8.9 ± 0.2
BG CMi	$6.43^{+0.07}_{-0.10}$	$6.62^{+0.22}_{-0.07}$	$6.88^{+0.23c}_{-0.07}$	$4.3^{+1.7}_{-1.8}$	$1.0^{+2.3}_{-1.0}$	$4.3^{+1.5}_{-4.3}$	120^{+50}_{-50}	31^{+70}_{-31}	140^{+50}_{-140}	35^{+30}_{-35}	$8.6^{+4.2}_{-4.2}$	20^{+23}_{-8}	28.9 ± 5.8
V1223 Sgr	$6.37^{+0.03}_{-0.02}$	$6.66^{+0.04}_{-0.04}$	$6.96^{+0.04}_{-0.03}$	14^{+2}_{-2}	11^{+2}_{-2}	$9.4^{+2.1}_{-2.3}$	110^{+20}_{-20}	87^{+18}_{-19}	82^{+19}_{-21}	12^{+2}_{-2}	11^{+2}_{-2}	23^{+18}_{-7}	29.0 ± 3.6
RX1712–24	$6.44^{+0.04}_{-0.05}$	$6.71^{+0.07}_{-0.06}$	$7.06^{+0.09}_{-0.07}$	10^{+2}_{-3}	$8.9^{+2.4}_{-2.5}$	$5.1^{+1.8}_{-1.9}$	150^{+40}_{-40}	140^{+40}_{-40}	87^{+32}_{-33}	$9.1^{+2.1}_{-2.3}$	$8.8^{+2.6}_{-2.6}$	16^{+7}_{-4}	—
AO Psc	$6.38^{+0.03}_{-0.03}$	$6.64^{+0.04}_{-0.04}$	$6.88^{+0.05}_{-0.04}$	$8.2^{+1.6}_{-1.5}$	12^{+2}_{-2}	$3.5^{+1.6}_{-1.5}$	150^{+30}_{-30}	310^{+30}_{-40}	94^{+40}_{-40}	$6.6^{+1.3}_{-1.5}$	$4.3^{+2.8}_{-2.8}$	12^{+7}_{-3}	13.7 ± 0.6
RXJ0558+535	$6.35^{+0.07}_{-0.07}$	$6.68^{+0.28}_{-0.17}$	$6.94^{+0.28c}_{-0.17}$	$5.4^{+1.5}_{-1.9}$	$1.9^{+1.6}_{-1.9}$	$2.1^{+1.7}_{-1.0}$	150^{+50}_{-60}	58^{+49}_{-58}	71^{+57}_{-34}	$13^{+\infty}_{-5}$	22^{+5}_{-5}	$8.1^{+6.5}_{-2.5}$	—
FO Aqr	$6.37^{+0.29}_{-0.07}$	$6.56^{+0.09}_{-0.07}$	$6.83^{+0.10}_{-0.08}$	$8.4^{+3.0}_{-3.6}$	$7.3^{+3.1}_{-3.1}$	$6.2^{+2.5}_{-2.4}$	95^{+34}_{-41}	87^{+36}_{-37}	78^{+32}_{-30}	11^{+4}_{-4}	15^{+3}_{-3}	23^{+22}_{-8}	31.5 ± 5.0
RE0751+14	$6.41^{+0.03}_{-0.12}$	$6.79^{+0.10}_{-0.32}$	$7.06^{+0.11c}_{-0.34}$	$6.0^{+1.0}_{-3.7}$	$2.1^{+1.1}_{-1.2}$	$0.66^{+2.47}_{-0.66}$	190^{+30}_{-120}	72^{+37}_{-43}	24^{+90}_{-24}	$6.9^{+9.3}_{-6.9}$	$9.9^{+3.8}_{-3.9}$	22^{+28}_{-9}	20.0 ± 8.5
TV Col	$6.44^{+0.04}_{-0.04}$	$6.76^{+0.06}_{-0.06}$	$7.06^{+0.12}_{-0.12}$	13^{+3}_{-4}	12^{+3}_{-4}	$5.0^{+3.5}_{-2.9}$	170^{+30}_{-30}	170^{+40}_{-50}	80^{+50}_{-50}	$7.7^{+2.7}_{-2.7}$	$6.0^{+3.6}_{-3.7}$	18^{+14}_{-6}	24.5 ± 3.9
TX Col	$6.38^{+0.15}_{-0.15}$	$6.68^{+0.08}_{-0.07}$	$7.03^{+0.11}_{-0.13}$	$1.9^{+1.3}_{-1.2}$	$3.3^{+1.4}_{-1.5}$	$1.8^{+1.4}_{-1.4}$	110^{+70}_{-70}	200^{+90}_{-90}	120^{+90}_{-90}	$8.9^{+3.8}_{-4.9}$	10^{+9}_{-9}	11^{+28}_{-5}	—
XY Ari	$6.40^{+0.06}_{-0.05}$	$6.73^{+0.07}_{-0.03}$	$7.01^{+0.07c}_{-0.03}$	$3.1^{+0.9}_{-2.7}$	$3.2^{+1.0}_{-3.2}$	$0.42^{+3.76}_{-0.42}$	100^{+30}_{-90}	120^{+40}_{-120}	16^{+146}_{-16}	$4.9^{+9.9}_{-4.9}$	13^{+4}_{-3}	16^{+21}_{-6}	17^{+6i}_{-4}
AE Aqr	6.40^{b}	$6.70^{+0.14}_{-0.32}$	$6.97^{+0.15c}_{-0.33}$	$0.46^{+0.81}_{-0.46}$	$1.5^{+1.2}_{-1.4}$	$0.73^{+1.91}_{-0.73}$	330^{+590}_{-330}	1300^{+1100}_{-1300}	830^{+2150}_{-830}	$8.6^{+10.4}_{-8.6}$	< 36	$2.7^{+0.5}_{-0.5}$	—
GK Per (Qui.)	$6.41^{+0.16}_{-0.14}$	6.64^{b}	6.91^{c}	$2.4^{+2.2}_{-1.8}$	$2.7^{+0.8}_{-2.7}$	< 2.7	47^{+43}_{-36}	58^{+17}_{-58}	< 61	—	$5.7^{+4.8}_{-4.8}$	14^{+26}_{-6}	32.0 ± 6.1
GK Per (Outb.)	$6.36^{+0.02}_{-0.02}$	$6.70^{+0.05}_{-0.06}$	$7.03^{+0.13}_{-0.12}$	76^{+8}_{-8}	42^{+8}_{-10}	17^{+10}_{-7}	160^{+20}_{-20}	94^{+18}_{-23}	43^{+24}_{-18}	$7.8^{+2.1}_{-1.8}$	29^{+2}_{-2}	16^{+8}_{-4}	15.5 ± 9.5

[a] In the unit of 10^{-5} photons cm^{-2} sec^{-1}.

[b] Fixed.

[c] Fixed at ×1.04 of He-like iron energy.

[d] Ionization temperature obtained from the intensity ratio of He-like and hydrogenic iron $K\alpha$ lines based on Mewe et al. (1985).

[e] Hydrogen column density determined from iron $K-$edge.

[f] Continuum Temperature measured by *ASCA* (ref. Fig. 2).

[g] Continuum Temperature measured by *Ginga*.

[h] Observed on 1989 September.

[i] Observed on 1987 July.

TABLE 3

BEST FIT PARAMETERS IN THE FULL ENERGY BAND BY THE MODEL OF THE THERMAL BREMSSTRAHLUNG UNDERGOING THE PARTIAL-COVERING ABSORPTION.

Source	Brems	Absorption			Flux[c]	Bolometric	χ_ν^2 (d.o.f.)		Fluorescent Iron Line	
	kT [keV]	N_{H1} [10^{22} cm^{-2}] Covering Fract.	N_{H2} [10^{22} cm^{-2}] Covering Fract.	N_{H3} [10^{22} cm^{-2}] Covering Fract.	Absorbed Intrinsic	Luminosity[d] [10^{32} erg s^{-1}]			$N_{H,eff}$ [10^{22} cm^{-2}]	observed E.W. [eV]
Polars										
EF Eri	16.9[a]	0.015 ± 0.009	3.3 ± 0.7	—	4.5 ± 0.1	1.2 ± 0.1	0.922	(348)	1.0 ± 0.2	30^{+32}_{-30}
		0.69 ± 0.02	0.69 ± 0.02	—	4.8 ± 0.1					
VV Pup	15.0[b]	0.0	22 ± 96	—	0.11 ± 0.03	0.033 ± 0.009	0.526	(99)	8.9 ± 38.9	150^{+480}_{-150}
		0.60 ± 0.19	0.40 ± 0.33	—	0.15 ± 0.04					
V834 Cen	14.7[a]	0.035 ± 0.027	2.2 ± 1.4	—	0.94 ± 0.05	0.21 ± 0.01	0.557	(229)	0.60 ± 0.40	79^{+135}_{-79}
		0.73 ± 0.06	0.27 ± 0.06	—	0.98 ± 0.05					
RXJ1802+1804	0.12 ± 0.02	0.98 ± 0.20	—	—	0.050 ± 0.018	21 ± 6	0.989	(64)	0.98 ± 0.20	1300^{+1300}_{-1300}
	4.7 ± 3.9	1.0	—	—	0.054 ± 0.019	0.0079 ± 0.0071				
BL Hyi	20.0[b]	0.061 ± 0.011	—	—	0.80 ± 0.01	0.19 ± 0.01	0.772	(294)	0.061 ± 0.011	96^{+103}_{-96}
		1.0	—	—	0.80 ± 0.01					
RX2107-05	10.0[b]	0.0059 ± 0.0526	6.5 ± 11.0	—	0.16 ± 0.09	0.037 ± 0.021	0.341	(31)	3.6 ± 6.2	530^{+650}_{-530}
		0.45 ± 0.18	0.55 ± 0.18	—	0.20 ± 0.11					
QS Tel	5.0[b]	0.040 ± 0.088	—	—	0.075 ± 0.010	0.015 ± 0.002	0.375	(42)	0.040 ± 0.088	< 3300
		1.0	—	—	0.076 ± 0.010					
AM Her	10.0[b]	0.0024 ± 0.0108	3.2 ± 0.5	36 ± 7	3.8 ± 0.3	1.4 ± 0.1	0.909	(294)	21 ± 5	170^{+40}_{-40}
(1993/09)		0.22 ± 0.02	0.20 ± 0.03	0.58 ± 0.10	7.0 ± 0.6					
AM Her	20.0[b]	0.018 ± 0.012	3.6 ± 0.6	28 ± 7	5.3 ± 0.3	1.9 ± 0.1	1.34	(298)	12 ± 3	220^{+30}_{-30}
(1995/03)		0.36 ± 0.02	0.24 ± 0.03	0.40 ± 0.05	7.7 ± 0.4					
BY Cam	30.0[a]	0.13 ± 0.01	3.0 ± 0.8	—	4.7 ± 0.1	1.5 ± 0.1	0.857	(257)	0.83 ± 0.10	81^{+33}_{-34}
		0.77 ± 0.02	0.23 ± 0.02	—	5.0 ± 0.1					
QQ Vul	41.9[a]	0.0	16 ± 20	—	0.31 ± 0.16	0.13 ± 0.07	0.622	(126)	6.4 ± 8.6	54^{+513}_{-54}
		0.61 ± 0.22	0.39 ± 0.22	—	0.39 ± 0.20					

TABLE 3—*Continued*

Source	Brems	Absorption			Flux[c]	Bolometric	χ_ν^2 (d.o.f.)		Fluorescent Iron Line	
	kT [keV]	N_{H1} [10^{22} cm^{-2}] Covering Fract.	N_{H2} [10^{22} cm^{-2}] Covering Fract.	N_{H3} [10^{22} cm^{-2}] Covering Fract.	Absorbed Intrinsic	Luminosity[d] [10^{32} erg s^{-1}]			$N_{H,eff}$ [10^{22} cm^{-2}]	observed E.W. [eV]
Intermediate Polars										
EX Hya	0.224 ± 0.008	0.48 ± 0.03	—	—	7.6 ± 1.8	25 ± 6	1.88	(377)	0.48 ± 0.03	91^{+71}_{-36}
	7.60 ± 0.45	1.0	—	—	7.9 ± 1.9	1.4 ± 0.1				
BG CMi	28.9[a]	0.37 ± 0.24	3.4 ± 0.6	18 ± 4	1.8 ± 0.1	0.87 ± 0.7	0.783	(205)	11 ± 2	120^{+50}_{-50}
		0.035 ± 0.019	0.42 ± 0.07	0.54 ± 0.07	2.8 ± 0.2					
V1223 Sgr	20.0[b]	0.032 ± 0.011	2.4 ± 0.2	21 ± 4	8.2 ± 0.3	2.9 ± 0.1	1.09	(394)	9.1 ± 1.5	110^{+20}_{-20}
		0.21 ± 0.01	0.41 ± 0.03	0.38 ± 0.03	11 ± 1					
RX1712–24	15.0[b]	0.11 ± 0.01	2.1 ± 0.2	27 ± 2	4.3 ± 0.2	1.4 ± 0.1	1.14	(319)	10 ± 1	150^{+40}_{-40}
		0.41 ± 0.03	0.23 ± 0.02	0.36 ± 0.04	5.9 ± 0.3					
AO Psc	13.7[a]	0.14 ± 0.02	2.9 ± 0.3	19 ± 4	3.9 ± 0.2	1.2 ± 0.1	1.12	(320)	7.7 ± 1.6	150^{+30}_{-30}
		0.22 ± 0.02	0.44 ± 0.04	0.34 ± 0.04	5.4 ± 0.3					
RXJ0558+535	10.0[b]	0.0	3.1 ± 0.4	34 ± 8	1.7 ± 0.2	0.60 ± 0.6	0.841	(289)	19 ± 6	150^{+50}_{-60}
		0.22 ± 0.02	0.25 ± 0.03	0.53 ± 0.11	3.0 ± 0.3					
FO Aqr	31.5[a]	0.20 ± 0.11	4.0 ± 0.7	25 ± 4	3.5 ± 0.2	2.3 ± 0.1	1.11	(174)	18 ± 3	95^{+34}_{-41}
		0.033 ± 0.009	0.27 ± 0.05	0.70 ± 0.06	6.6 ± 0.4					
RE0751+14	20.0[a]	0.0	2.0 ± 0.4	23 ± 5	2.2 ± 0.1	0.81 ± 0.05	0.949	(364)	11 ± 3	190^{+30}_{-120}
		0.30 ± 0.02	0.23 ± 0.03	0.47 ± 0.06	3.2 ± 0.2					
TV Col	24.5[a]	0.11 ± 0.02	2.8 ± 0.3	23 ± 5	4.9 ± 0.3	1.9 ± 0.1	0.909	(354)	10 ± 2	170^{+30}_{-30}
		0.20 ± 0.02	0.40 ± 0.04	0.40 ± 0.05	7.0 ± 0.4					
TX Col	10.0[b]	0.023 ± 0.023	2.3 ± 0.7	29 ± 10	1.2 ± 0.2	0.41 ± 0.06	0.659	(304)	17 ± 7	110^{+70}_{-70}
		0.20 ± 0.03	0.23 ± 0.05	0.57 ± 0.16	2.1 ± 0.3					
XY Ari	17.0[a]	3.7 ± 0.7	7.5 ± 6.2	70 ± 36	1.7 ± 0.5	0.77 ± 0.24	0.883	(267)	30 ± 22	100^{+30}_{-90}
		0.33 ± 0.18	0.30 ± 0.20	0.38 ± 0.24	3.3 ± 1.0					
AE Aqr	0.165 ± 0.020	0.59 ± 0.09	—	—	0.27 ± 0.03	18 ± 12	0.832	(174)	0.59 ± 0.09	330^{+590}_{-330}
	2.32 ± 0.28	1.0	—	—	0.29 ± 0.04	0.084 ± 0.011				
GK Per	32.0[a]	0.29 ± 0.19	1.5 ± 0.2	—	2.9 ± 0.1	1.1 ± 0.1	0.877	(334)	1.4 ± 0.2	47^{+43}_{-36}
(Qui.)		0.10 ± 0.06	0.90 ± 0.06	—	3.3 ± 0.1					
GK Per	15.0[b]	3.9 ± 0.6	14 ± 3	61 ± 9	19 ± 1	13 ± 1	0.832	(345)	42 ± 7	160^{+20}_{-20}
(Outb.)		0.096 ± 0.025	0.29 ± 0.04	0.61 ± 0.06	58 ± 4					

[a]Fixed at the value obtained by *Ginga*.
[b]Fixed at the value obtained by *ASCA* (either at 5, 10, 15, or 20 keV).
[c]Flux in the unit of 10^{-11} erg cm^{-2} sec^{-1} in 2.0–10 keV.
[d]Distance assumed to be 100 pc.

TABLE 4

IONIZATION TEMPERATURES, WHITE DWARF MASSES, AND ABUNDANCES.

Source	$kT_{\rm ion}$ [keV]	Mass [This Work] [$M_\odot$]	Mass [Cropper et al. (1998)] [$M_\odot$]	EW (summed) [keV]	Abundance [$\odot$]
Polar					
EF Eri	$8.8^{+3.9}_{-5.5}$	—	0.88 (0.82 – 0.94)	$0.16^{+0.06}_{-0.07}$	0.25 (0.14 – 0.35)
VV Pup	—	—	—	$0.12^{+0.49}_{-0.12}$	—
V834 Cen	$4.5^{+5.3}_{-4.5}$	—	0.51 (0.25 – 1.00)	$0.44^{+0.30}_{-0.21}$	0.34 (0.17 – 0.61)
RXJ1802–1804	$6.4^{+12.5}_{-6.4}$	—	—	$2.25^{+1.09}_{-1.05}$	2.22 (< 20)
BL Hyi	$9.4^{+5.6}_{-5.4}$	—	—	$0.62^{+0.29}_{-0.32}$	1.1 (0.50 – 2.10)
RX2107–05	—	—	—	$0.19^{+1.40}_{-0.19}$	—
QS Tel	—	—	—	$0.66^{+5.60}_{-0.66}$	—
AM Her (93/09)	$9.6^{+2.2}_{-2.5}$	—	1.22 (1.15 – 1.30)	$0.28^{+0.06}_{-0.06}$	0.53 (0.41 – 0.67)
AM Her (95/03)	$9.1^{+1.4}_{-1.5}$	—	1.22 (1.15 – 1.30)	$0.36^{+0.05}_{-0.05}$	0.61 (0.51 – 0.71)
BY Cam	16^{+10}_{-11}	—	1.06 (1.00 – 1.25)	$0.15^{+0.06}_{-0.09}$	— (0.05 – 1.26)
QQ Vul	$9.3^{+8.2}_{-9.3}$	—	1.12 (0.95 – 1.30)	$1.00^{+0.80}_{-0.80}$	1.80 (0.30 – 3.60)
Intermediate Polar					
EX Hya	$7.4^{+0.9}_{-0.9}$	0.48 (0.42 – 0.58)	0.52 (0.40 – 0.60)	$0.49^{+0.05}_{-0.07}$	0.72 (0.60 – 0.80)
BG CMi	35^{+36}_{-35}	—	1.22 (1.05 – 1.30)	$0.17^{+0.08}_{-0.14}$	— (< 1.5)
V1223 Sgr	12^{+2}_{-2}	1.28 (> 0.84)	—	$0.17^{+0.03}_{-0.03}$	0.68 (0.54 – 0.83)
RX1712–24	$9.1^{+2.1}_{-2.3}$	0.68 (0.42 – 1.10)	—	$0.23^{+0.05}_{-0.05}$	0.39 (0.30 – 0.48)
AO Psc	$6.6^{+1.3}_{-1.5}$	0.40 (0.30 – 0.53)	0.39 (< 0.80)	$0.40^{+0.05}_{-0.06}$	0.41 (0.30 – 0.55)
RXJ0558+53	$13^{+\infty}_{-5}$	> 0.54	—	$0.13^{+0.08}_{-0.07}$	0.78 (> 0.13)
FO Aqr	11^{+4}_{-4}	1.05 (> 0.44)	1.24 (> 1.0)	$0.17^{+0.05}_{-0.05}$	0.48 (0.33 – 0.64)
RE0751+14	$6.9^{+9.3}_{-6.9}$	—	1.35 (> 1.05)	$0.10^{+0.10}_{-0.05}$	0.10 (0.05 – 0.21)
TV Col	$7.7^{+2.7}_{-2.7}$	0.51 (0.29 – 0.92)	1.15 (> 0.95)	$0.25^{+0.07}_{-0.07}$	0.31 (0.22 – 0.41)
TX Col	$8.9^{+3.8}_{-4.9}$	0.66 (0.24 – 1.39)	0.55 (0.44 - 0.64)	$0.32^{+0.13}_{-0.13}$	0.52 (0.30 – 0.78)
XY Ari	$4.9^{+9.9}_{-4.9}$	—	—	$0.13^{+0.15}_{-0.12}$	0.10 (0.01 – 0.23)
AE Aqr	$8.6^{+10.4}_{-8.6}$	—	0.31 (< 1.15)	$2.10^{+2.40}_{-1.50}$	3.20 (0.60 – 7.50)
GK Per (Qui.)	—	—	—	$0.06^{+0.06}_{-0.06}$	—
GK Per (Otb.)	$7.8^{+2.1}_{-1.8}$	0.52 (0.36 – 0.86)	—	$0.14^{+0.03}_{-0.03}$	0.18 (0.14 – 0.22)

Fig. 1.— *ASCA* SIS spectra of mCVs in the band 5-10 keV. In the upper plot of each panel, crosses are the data points and the histogram is the model composed of the thermal bremsstrahlung undergoing the photoelectric absorption plus three Gaussian lines. The lower plot indicates fit residuals in the unit of σ. Note that although only the SIS results are shown, the fits are carried out simultaneously with the GIS and the SIS.

Fig. 2.— Examples of evaluating the continuum temperature for AM Her and TV Col. Each spectrum is fitted by the thermal bremsstrahlung with the photoelectric absorption represented by a single hydrogen column density in the band $E_{\rm LB}$–10 keV. If $E_{\rm LB}$ is low enough, the fitting results in a very high temperature due to a hardening by the partial-covering absorber. As we shift $E_{\rm LB}$ to higher energies, The temperature converges to a real value (see the text).

Fig. 3.— *ASCA* SIS spectra of mCVs in the full energy band. They are basically represented by a single temperature thermal bremsstrahlung undergoing a partial-covering absorption with two or three column densities. Exceptions are EX Hya, AE Aqr and RX J1802+1804 in which the spectrum requires multi-temperature thermal bremsstrahlung. In addition to iron emission lines, some spectra show evidence of other emission lines such as Ne, Mg, Si, S and Ar. For detail, see §§ 3.3. Note that although only the SIS spectra are shown, the fits are performed simultaneously with the SIS and the GIS.

Fig. 4.— (a) A scattered plot between the ionization temperature and the continuum temperature. The latter is generally higher than the former, indicating a temperature distribution in the post-shock hot plasma. The dotted line implies ionization temperature = continuum temperature. The dot-dash line is drawn with 40 % correction of the continuum temperature to the dotted line, which implies the correction for the hardening of the spectrum brought about by the reflection from the white dwarf. (b) The same plot as (a) but the continuum temperature is corrected to the shock temperature according to Wu et al. (1994,

1995). Dashed curves indicate predictions by Aizu model with the base temperature of 0, 2, and 4 keV.

Fig. 5.— Theoretical relation between the mass of the white dwarf and the ionization temperature expected from Aizu model. We show cases for the base temperature = 0, 2, 4 keV.

Fig. 6.— (a) A scattered plot between the ionization temperature and the summed equivalent width of the hydrogenic and He-like iron $K\alpha$ lines. Curves shown are relations expected from Aizu model with Solar abundance accreting matter with the base temperature of 0, 2, 4 keV. (b) Abundance Distribution.

Fig. 7.— (a) A scattered plot between the effective hydrogen column density and the equivalent width of the fluorescent iron $K\alpha$ emission line. Dotted lines show expected relations when a point-like thermal bremsstrahlung source is surrounded by a uniform absorber by 4π solid angle. (b) The same as (a) but the equivalent width of each source is corrected in the case of Solar abundance. The dashed curves represent the equivalent widths expected from the sum of contributions from the white dwarf surface and the line of sight absorber (eq.(10)).

Fig. 8.— Simulated relation between observed $N_{\rm H,eff}$ and $N_{\rm H}$ which is purely from the line of sight absorber ($N_{\rm H.cloud}$). It is possible that the observed $N_{\rm H,eff}$ includes the offset of $10^{22}{\rm cm}^{-2}$ brought about by the reflection from the white dwarf surface.

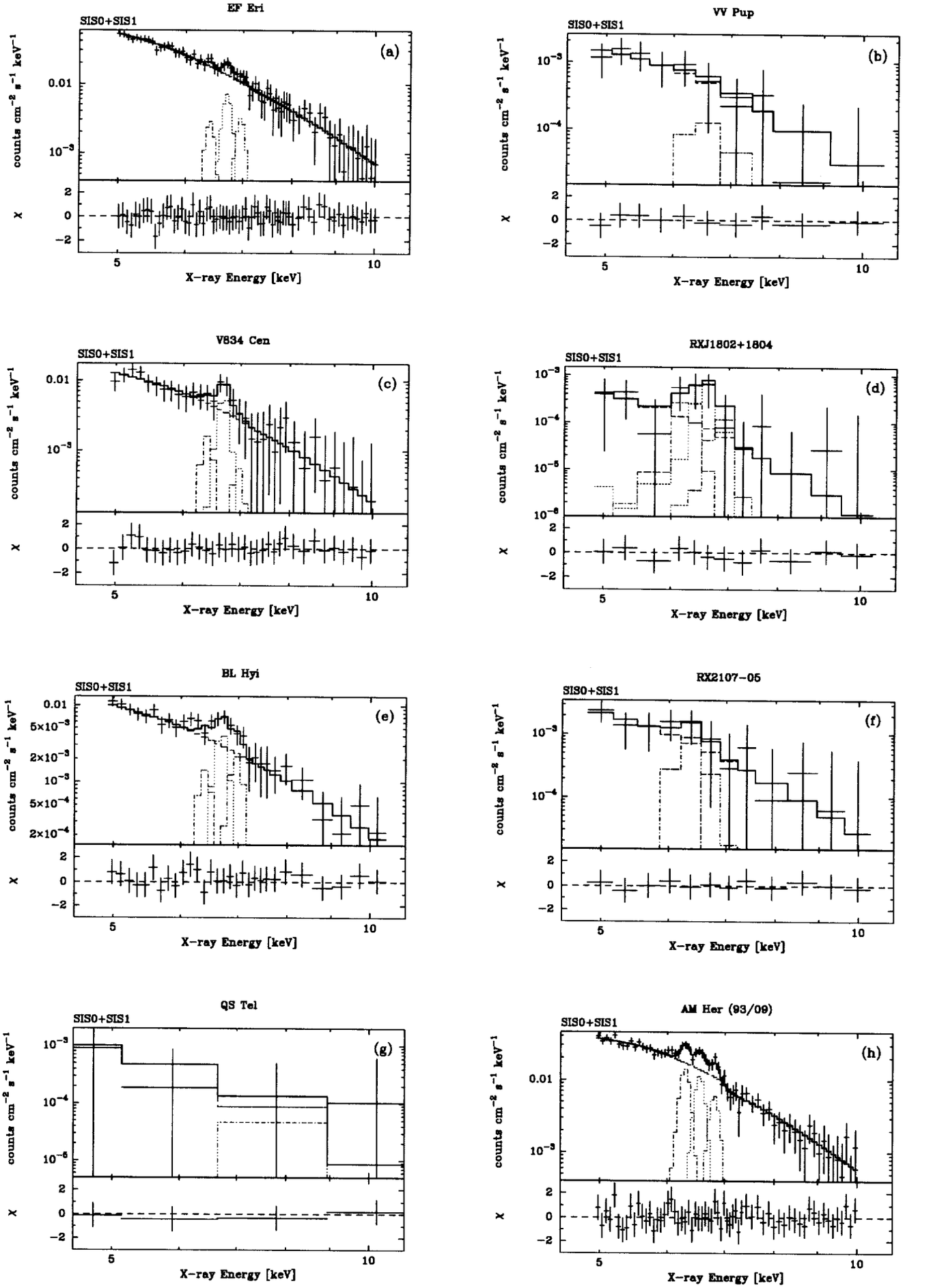
EF Eri
SIS0+SIS1
(a)
VV Pup
SIS0+SIS1
(b)
V834 Cen
SIS0+SIS1
(c)
RXJ1802+1804
SIS0+SIS1
(d)
BL Hyi
SIS0+SIS1
(e)
RX2107-05
SIS0+SIS1
(f)
QS Tel
SIS0+SIS1
(g)
AM Her (93/09)
SIS0+SIS1
(h)
counts cm^{-2} s^{-1} keV^{-1}
χ
X-ray Energy [keV]

Figure 1:

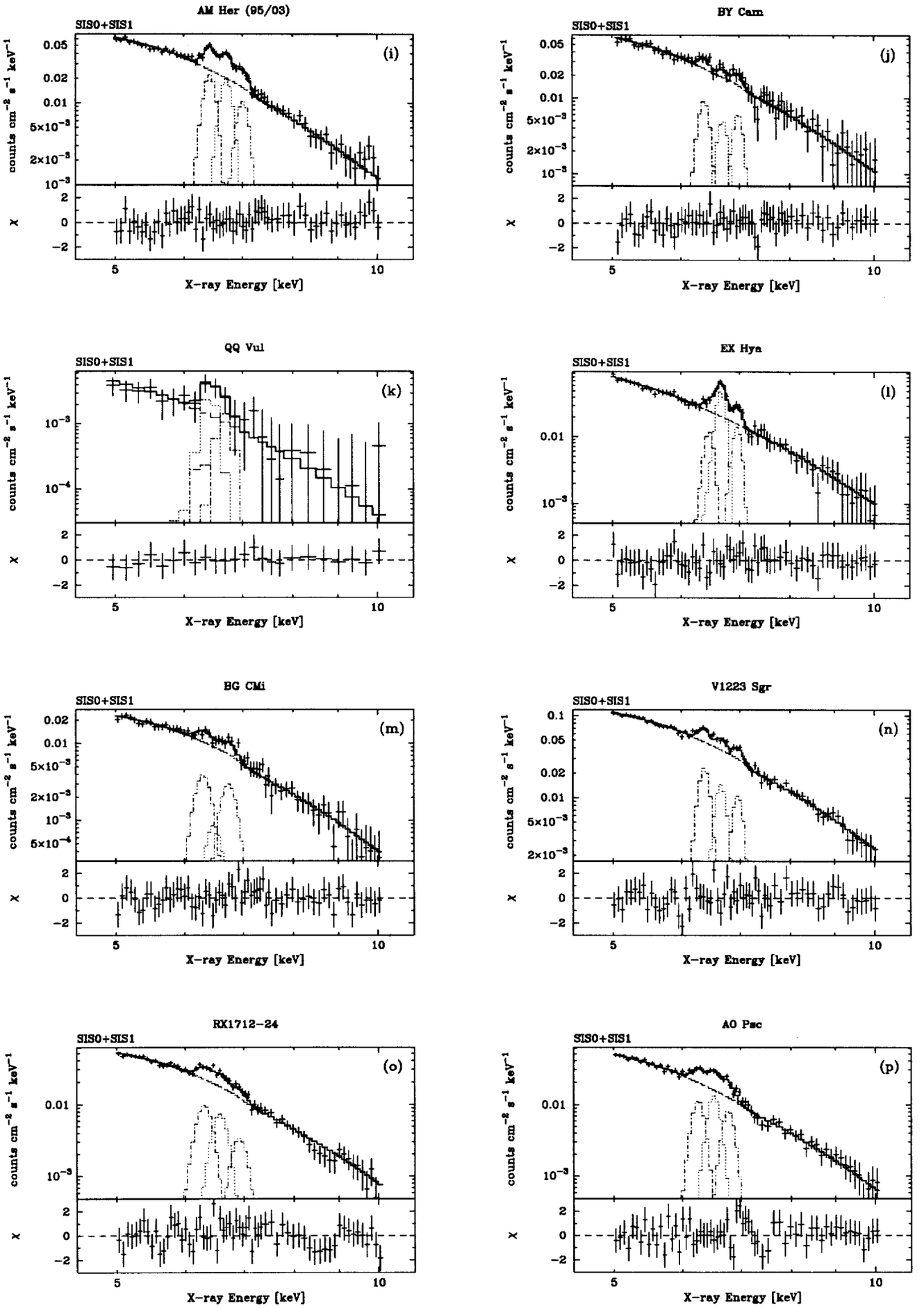

Figure 1: (continued)

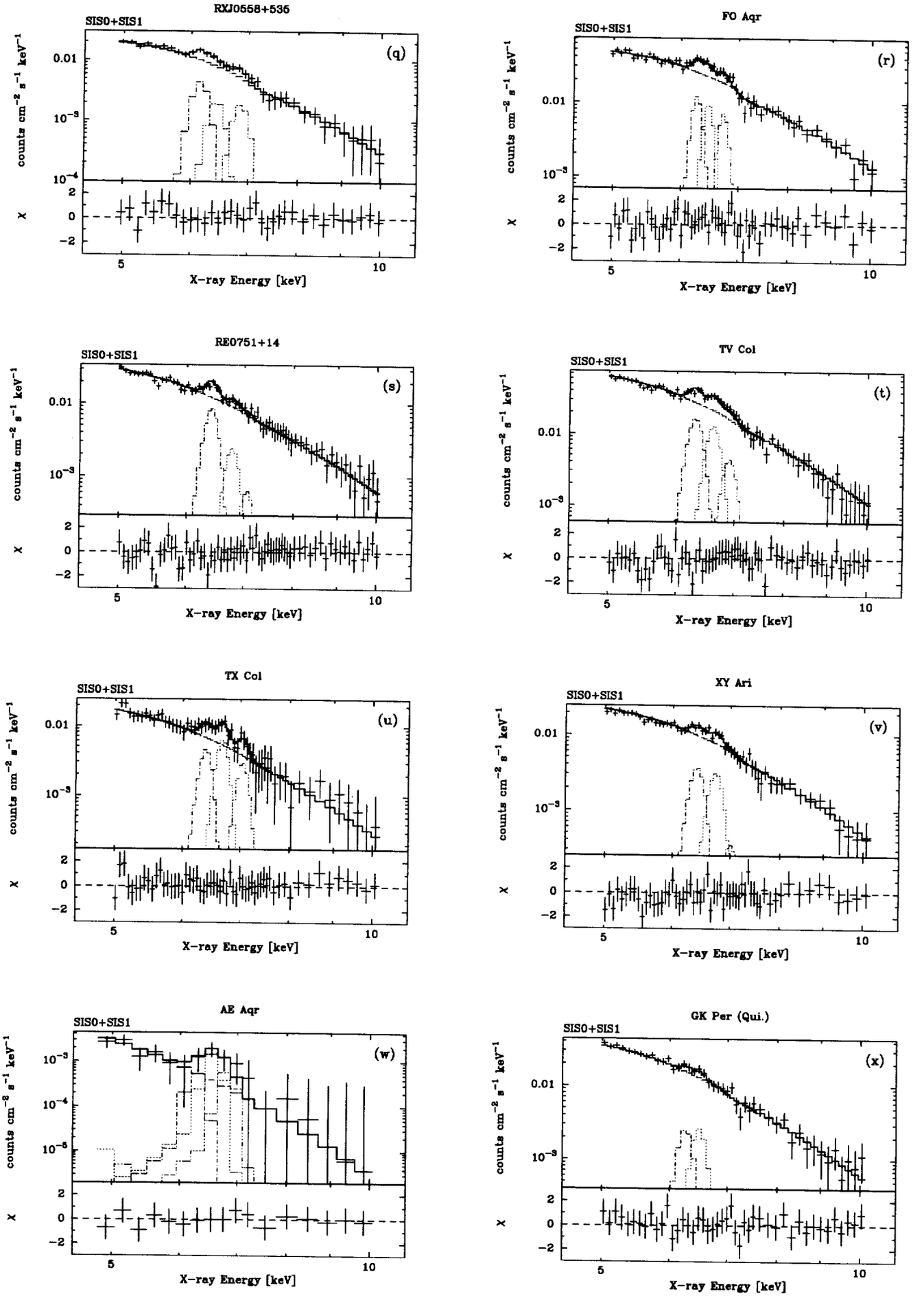

Figure 1: (continued)

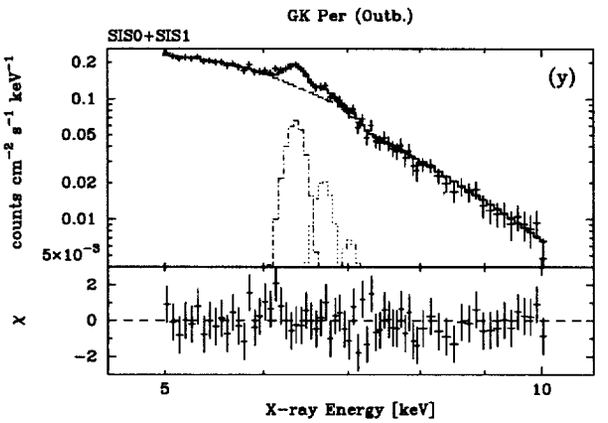

Figure 1: (continued)

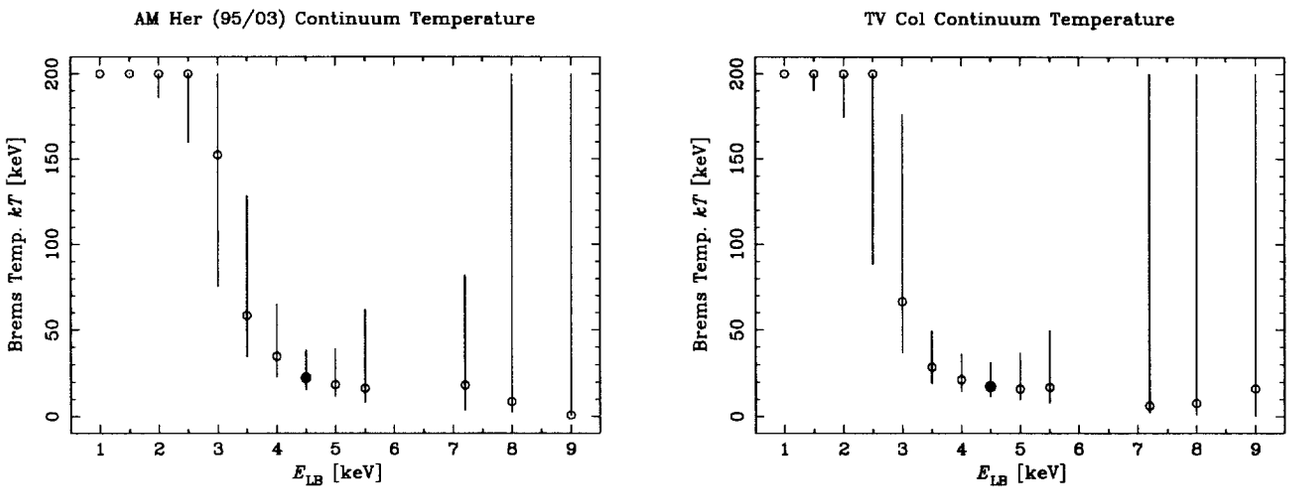

Figure 2:

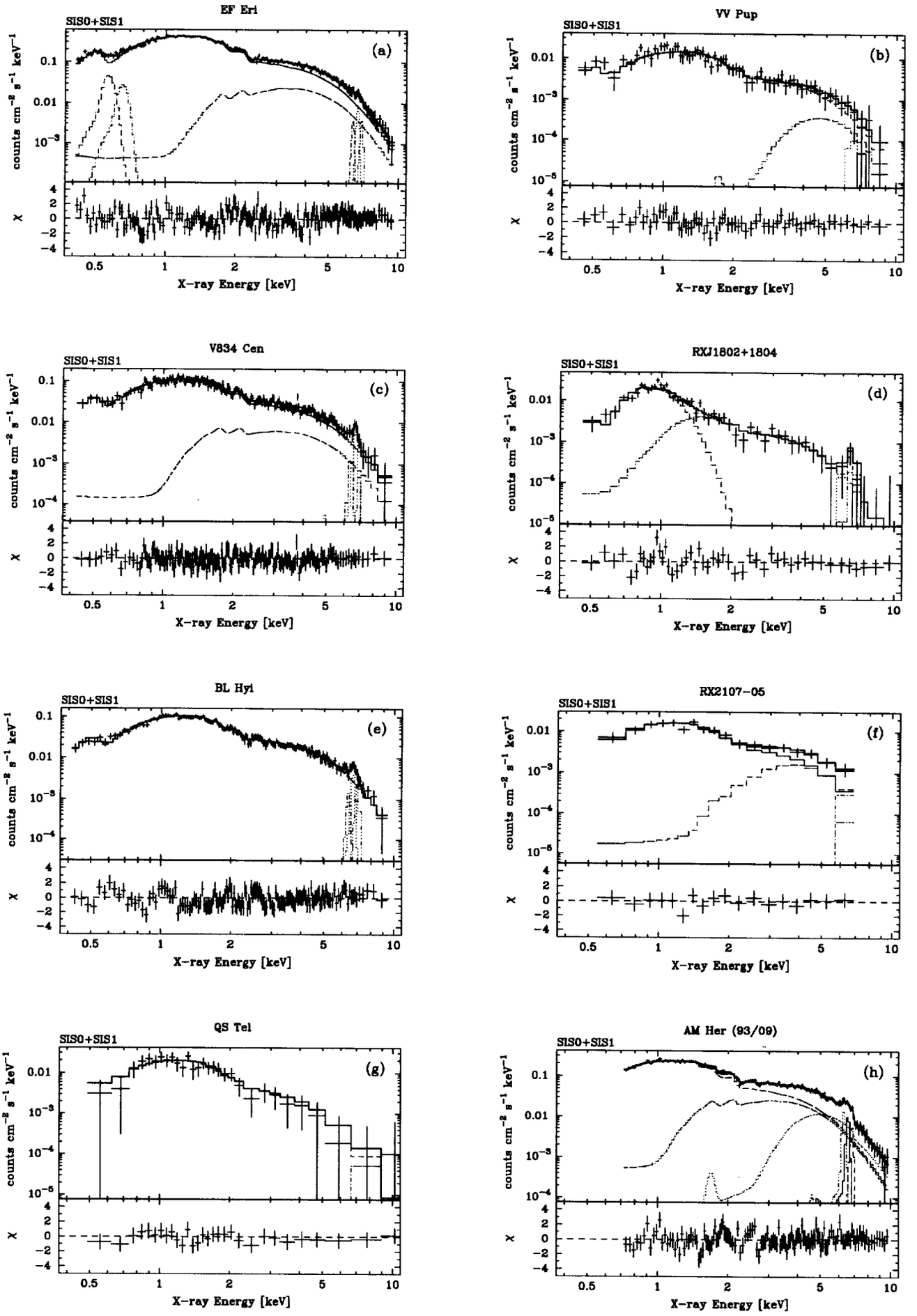
EF Eri
SIS0+SIS1
(a)
VV Pup
SIS0+SIS1
(b)
V834 Cen
SIS0+SIS1
(c)
RXJ1802+1804
SIS0+SIS1
(d)
BL Hyi
SIS0+SIS1
(e)
RX2107-05
SIS0+SIS1
(f)
QS Tel
SIS0+SIS1
(g)
AM Her (93/09)
SIS0+SIS1
(h)
counts cm^{-2} s^{-1} keV^{-1}
χ
X-ray Energy [keV]

Figure 3:

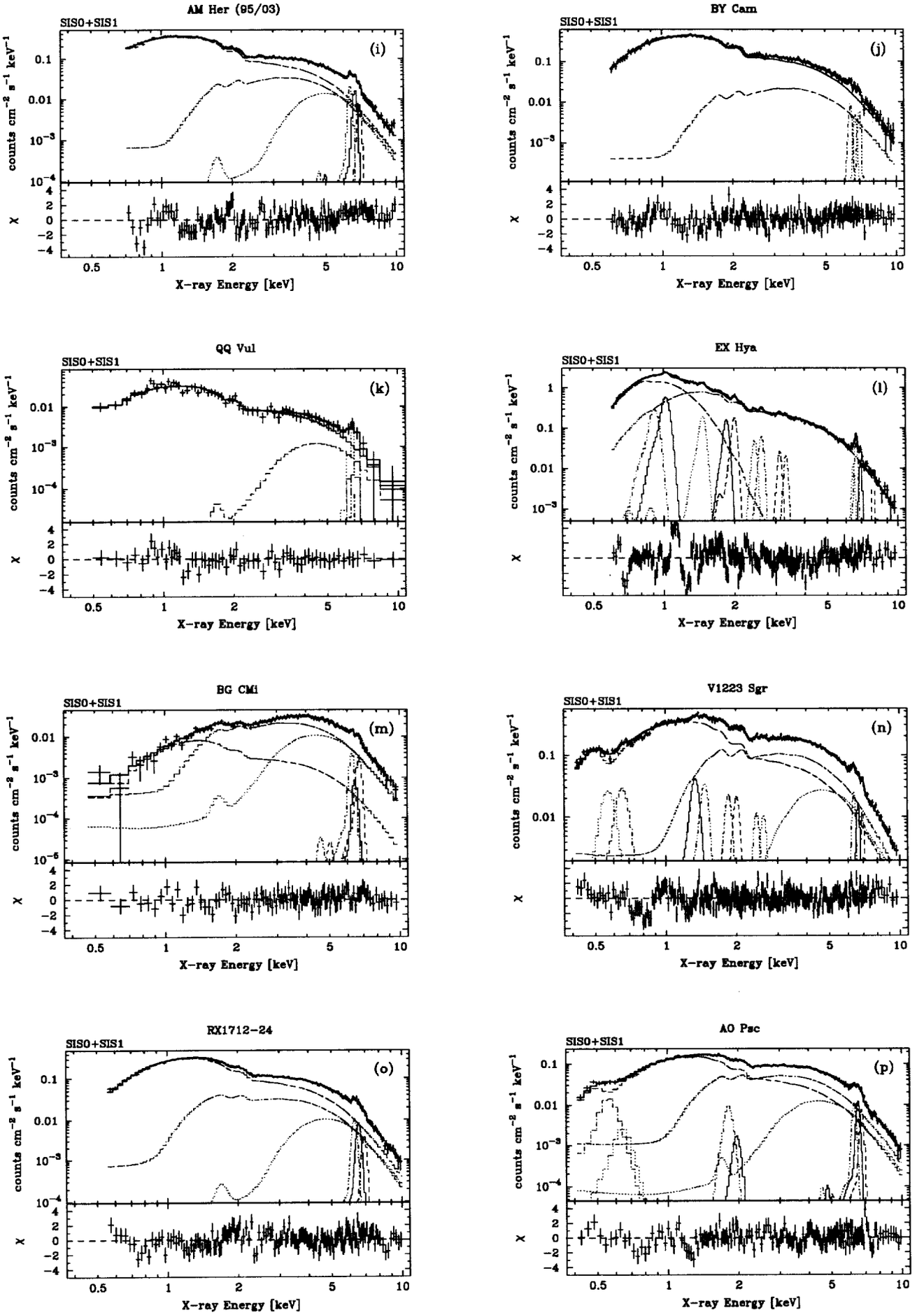

Figure 3: (cont'd).

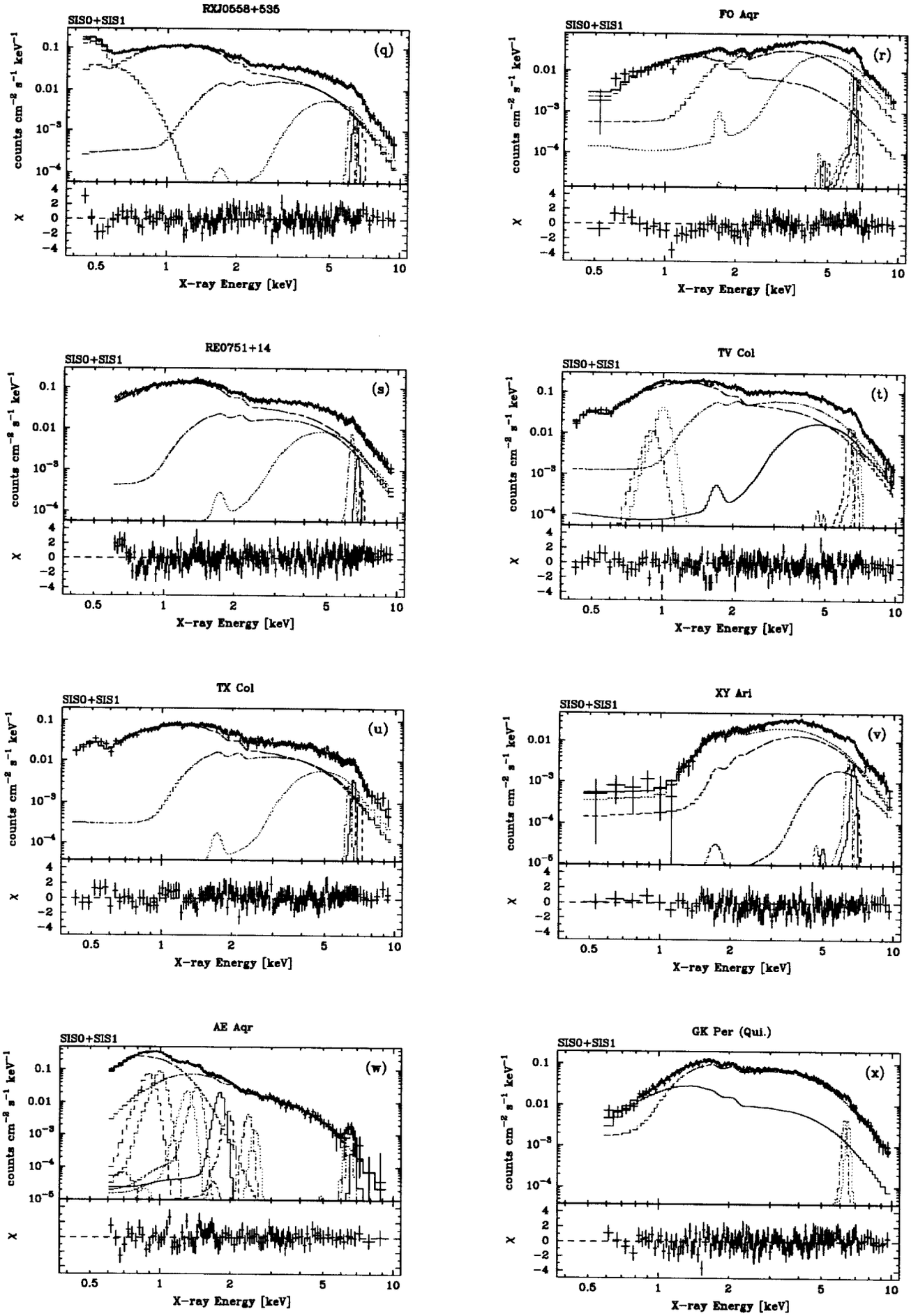

Figure 3: (cont'd).

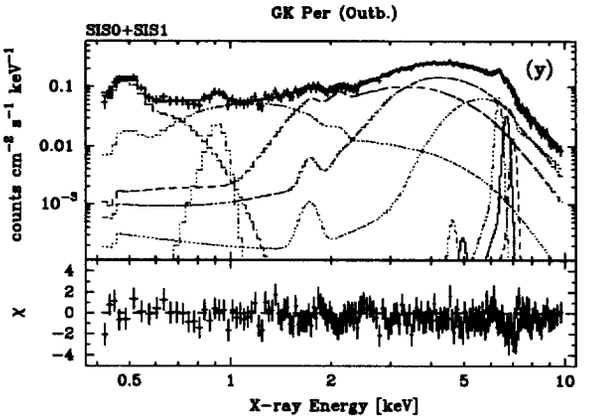

Figure 3: (cont'd).

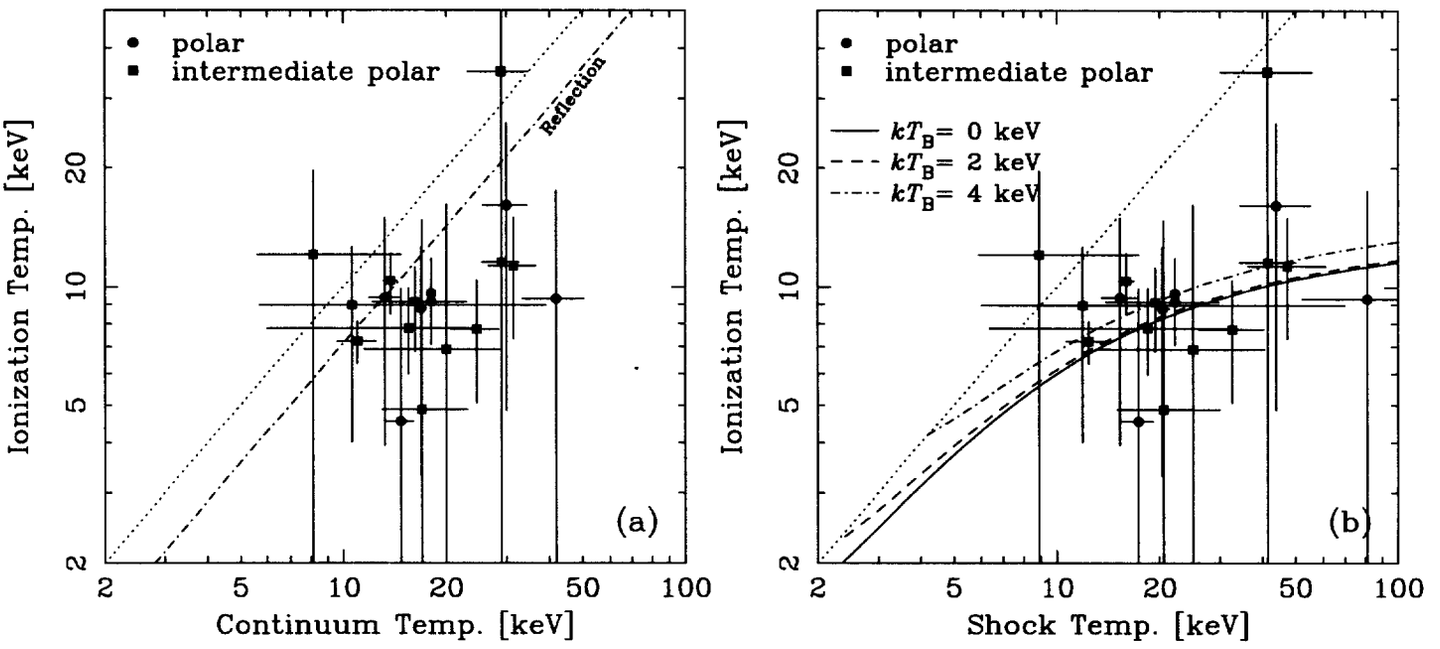

Figure 4:

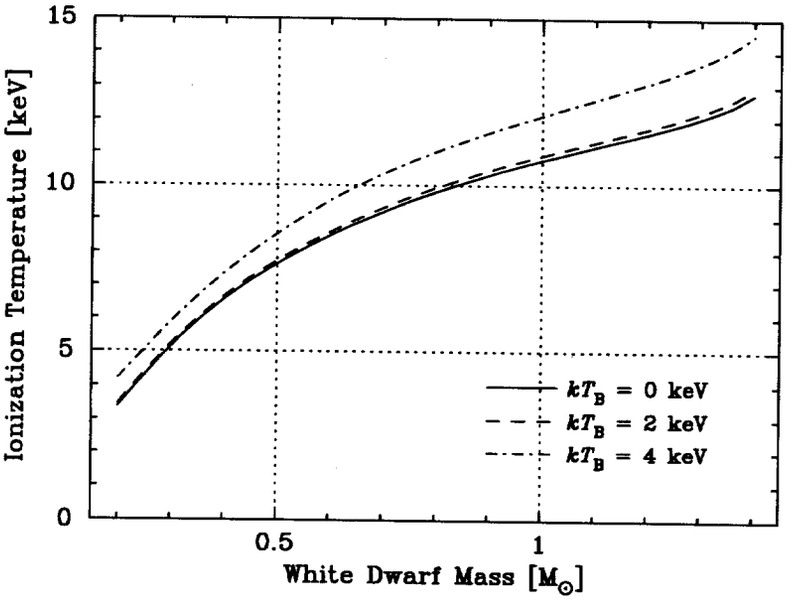

Figure 5:

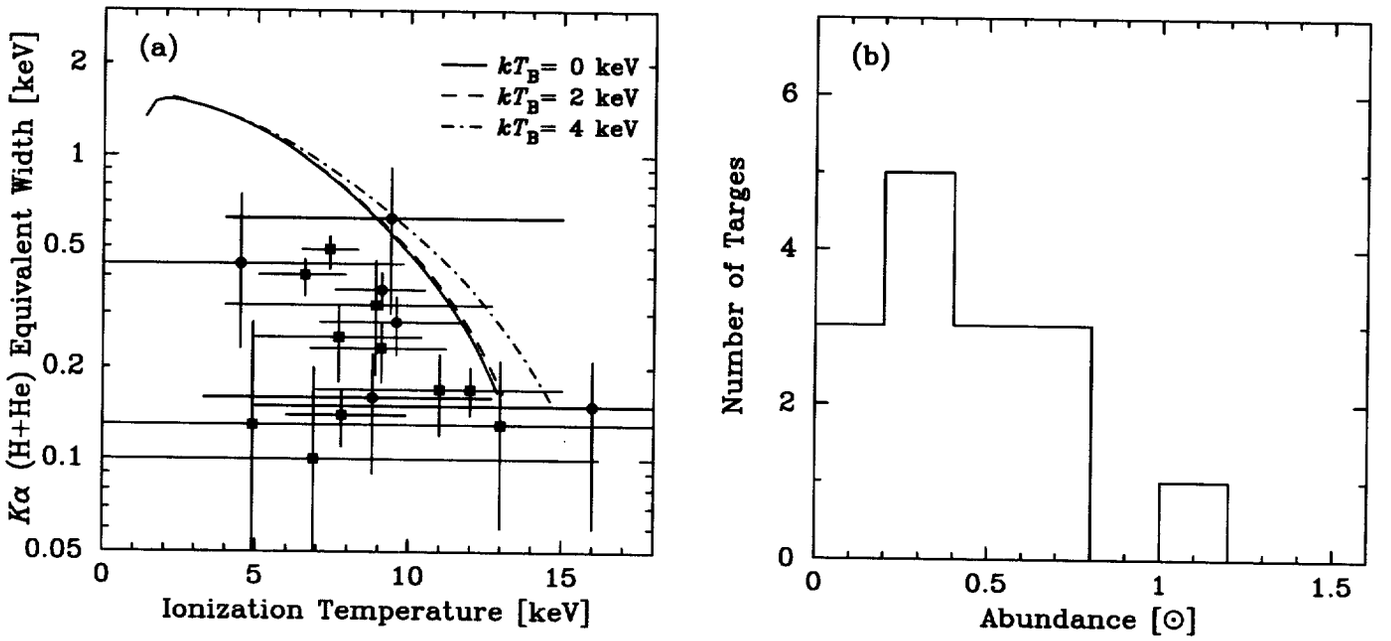

Figure 6:

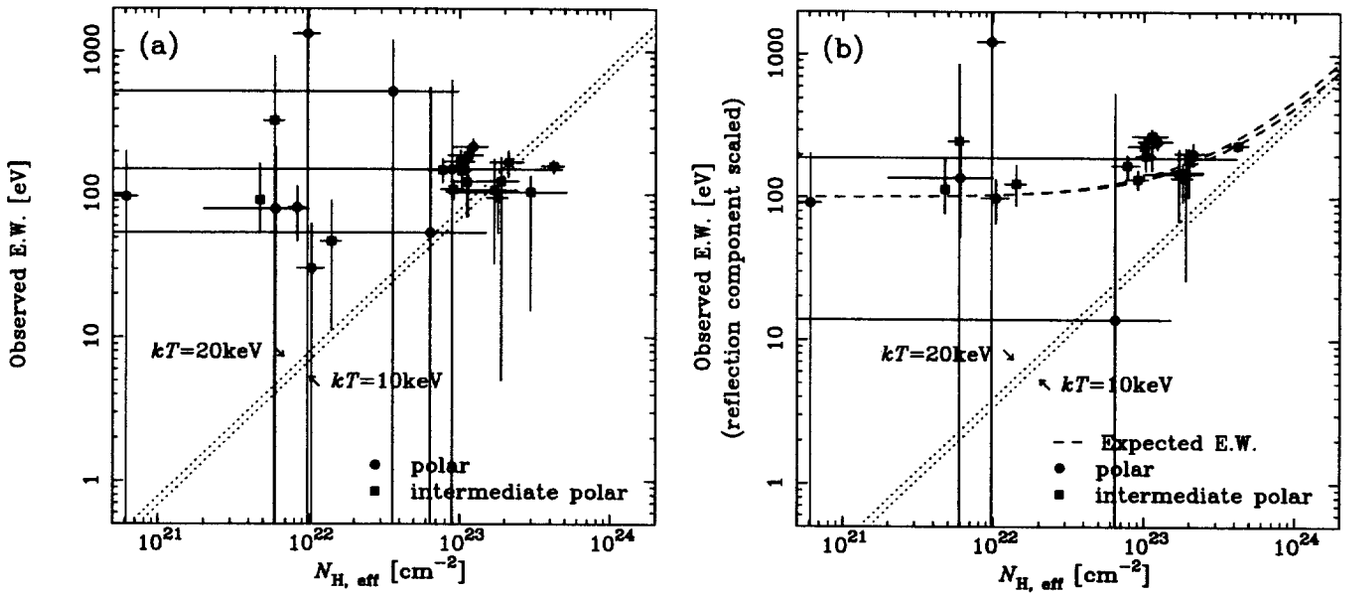

Figure 7:

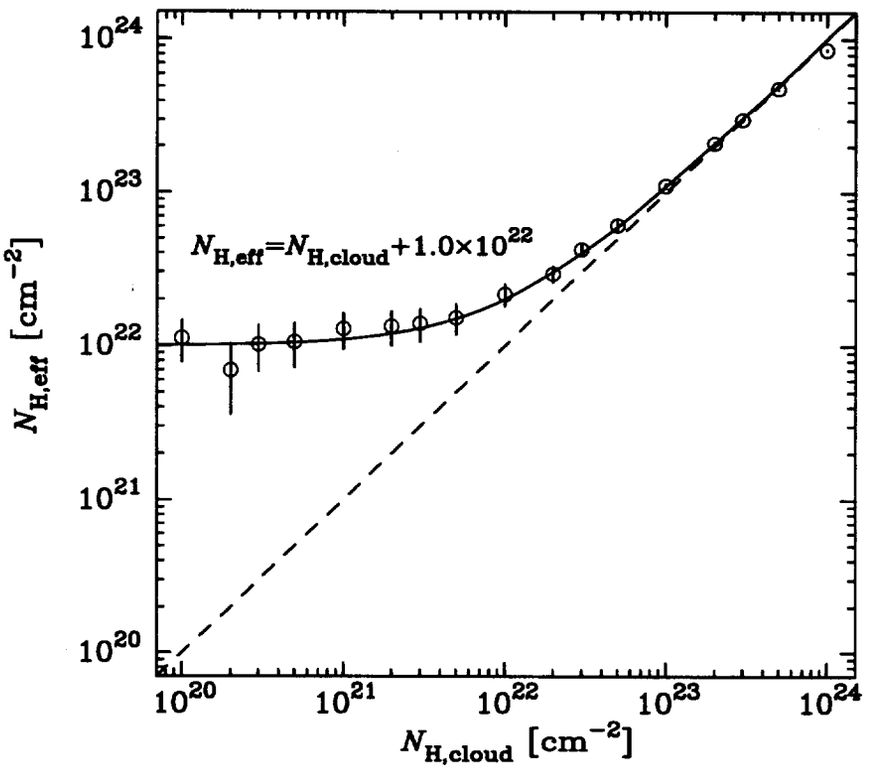

Figure 8: